

¹
² Susceptible host dynamics explain pathogen resilience to
³ perturbations

⁴
⁵ Sang Woo Park, . . . , Bryan T. Grenfell, Sarah Cobey

⁶ Abstract

⁷ Major priority for epidemiological research in the time of anthropogenic change is un-
⁸ derstanding how infectious disease dynamics respond to perturbations. Interventions
⁹ to slow the spread of SARS-CoV-2 significantly disrupted the transmission of other
¹⁰ human pathogens. As interventions lifted, whether and when respiratory pathogens
¹¹ would eventually return to their pre-pandemic dynamics remains to be answered. We
¹² develop a framework for estimating pathogen resilience based on how fast epidemic
¹³ patterns return to their pre-pandemic, endemic dynamics. Our analysis suggests
¹⁴ that some pathogens may have settled to endemic cycles that are different from their
¹⁵ pre-pandemic patterns. Finally, we show that the replenishment rate of the suscep-
¹⁶ tible pool is a key determinant of pathogen resilience. Our framework offers a novel
¹⁷ perspective to characterizing the dynamics of endemic pathogens and their responses
¹⁸ to SARS-CoV-2 interventions. **[SWP: Need to emphasize broader implications.]**

19 Non-pharmaceutical interventions (NPIs) to slow the spread of SARS-CoV-2 dis-
 20 rupted the transmission of other human respiratory pathogens, adding uncertainties
 21 to their future epidemic dynamics and the overall public health burden [1]. As
 22 NPIs lifted, large heterogeneities in outbreak dynamics were observed across differ-
 23 ent pathogens in different countries, with some pathogens exhibiting earlier resur-
 24 gences than others [2, 3, 4]. Heterogeneities in the overall reduction in transmission
 25 and the timing of re-emergence likely reflect differences in NPI patterns, pathogen
 26 characteristics, immigration/importation from other countries, and pre-pandemic
 27 pathogen dynamics [5]. Therefore, comparing the differential impact of the pandemic
 28 NPIs across pathogens can provide unique opportunities to learn about underlying
 29 pathogen characteristics, such as their transmissibility or duration of immunity, from
 30 heterogeneities in re-emergence patterns [6].

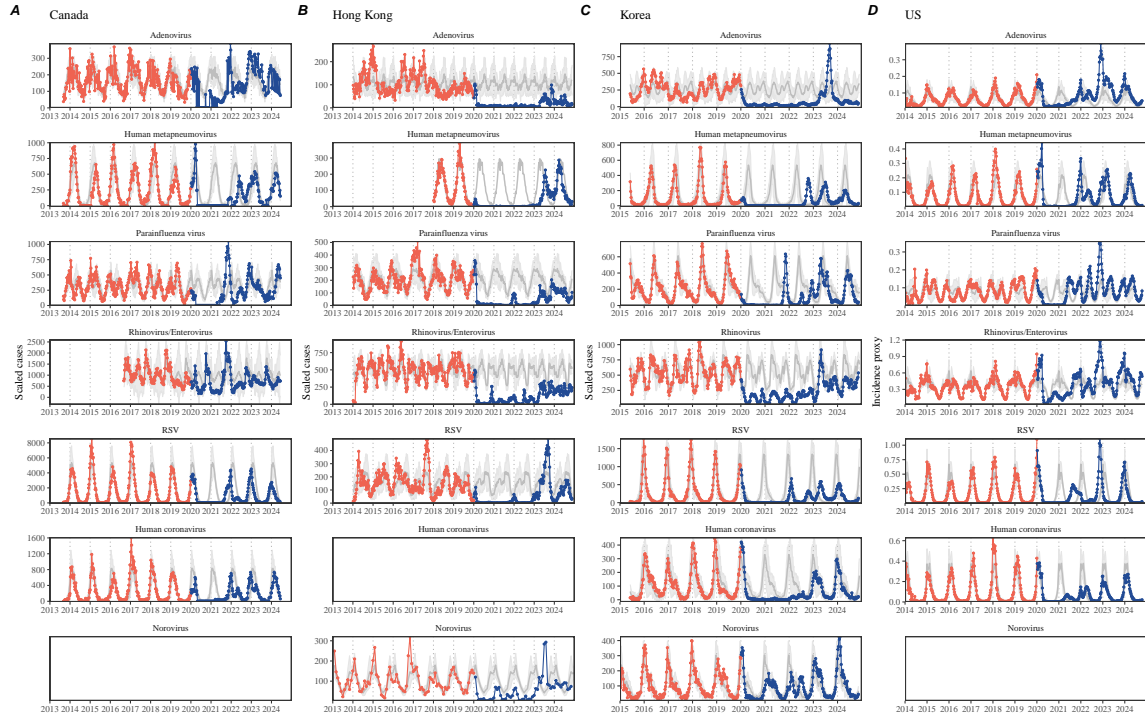


Figure 1: Observed heterogeneity in responses to pandemic NPIs across respiratory pathogens and norovirus in (A) Canada, (B) Hong Kong, (C) Korea, and (D) US. Red points and lines represent data before 2020. Blue points and lines represent data since 2020. Gray lines and shaded regions represent the mean seasonal patterns and corresponding 95% confidence intervals around the mean. Mean seasonal patterns were calculated by aggregating cases before 2020 into 52 weekly bins and taking the average in each week. Cases were scaled to account for changes in testing patterns (Materials and Methods).

31 Even though more than five years have passed since the emergence of SARS-CoV-
 32 2, we still observe persistent changes in pathogen dynamics following the pandemic

NPIs: for example, compared to pre-pandemic, seasonal patterns, human metapneumovirus in Korea seem to circulate at lower levels, whereas RSV in Korea seem to exhibit different seasonality (Figure 1). These observations suggest a possibility for a fundamental change in pathogen dynamics following the pandemic NPIs, which can be driven by permanent shift in either human behavior or population-level immunity [7, 8]. The possibility of a long-lasting impact of the pandemic NPIs pose an important question for future infectious disease dynamics: can we predict whether and when other respiratory pathogens will eventually return to their pre-pandemic dynamics? **[SWP: You suggested: I would say something about the dynamics of these pathogens not being well understood, but I've since rewritten the most of intro and I'm not sure where I would fit this. If you have any suggestions, let me know...]**

So far, the majority of epidemiological analyses of respiratory pathogens in the context of the pandemic NPIs have focused on characterizing the timing of rebound [1, 9, 5]. Instead, we seek to characterize how fast a pathogen returns to its pre-pandemic dynamics. These two concepts have subtle but important differences: for example, it took more than 3 years for human metapneumovirus to rebound in Hong Kong but the observed epidemic patterns in 2024 are similar to pre-pandemic seasonal means, suggesting a rapid return to pre-pandemic dynamics following a perturbation (Figure 1). Measuring this rate of return is particularly useful because it allows us to quantify the ecological resilience of a host-pathogen system [10, 11, 12, 13].

In this study, we lay out theoretical and statistical approaches to characterizing the resilience of a host-pathogen system based on how fast the system recovers from perturbation. We begin by laying out a few representative scenarios that capture the potential impact of NPIs on endemic pathogen dynamics and illustrate how resilience can be measured by comparing the pre- and post-pandemic dynamics of susceptible and infected hosts. In practice, information on susceptible hosts is often unavailable, making this theoretical approach infeasible. Instead, we utilize a mathematical technique to reconstruct empirical attractors from the data [14], which allows us to measure the rate at which the host-pathogen system approaches this empirical attractor after a perturbation; this rate corresponds to the resilience of the host-pathogen system. We use this method to analyze pathogen surveillance data for respiratory and non-respiratory pathogens from Canada, Hong Kong, Korea, and US. Finally, we show that susceptible host dynamics explain variation in pathogen resilience.

Conceptual introduction to pathogen resilience

In classical ecological literature, resilience of an ecological system is measured by the rate at which the system returns to its reference state following a perturbation [10, 11, 12, 13]. This rate corresponds to the largest real part of the eigenvalues of the linearized system near equilibrium—here, we refer to this value as the *intrinsic* resilience of the system, which represents the expected rate of return from perturbed states. In practice, we rarely know the true model describing population-level dy-

73 namics of common respiratory pathogens, limiting our ability to infer the intrinsic
74 resilience of a system. Instead, we can still measure the *empirical* resilience of a
75 host-pathogen system by looking at how fast the system returns to the pre-pandemic,
76 endemic dynamics after interventions are lifted.

77 As an example, we begin with a simple Susceptible-Infected-Recovered-Susceptible
78 (SIRS) model with seasonally forced transmission and demography (i.e., birth and
79 death). The SIRS model is the simplest model that allows for waning of immunity
80 and is commonly used for modeling the dynamics of respiratory pathogens [15]. First,
81 consider an intervention that reduce transmission by 50% for 6 months starting in
82 2020, which causes epidemic patterns to deviate from its original stable annual cycle
83 for a short period of time and eventually come back (Figure 2A). To measure the
84 resilience of this system empirically, we first need to be able to measure the dis-
85 tance from its pre-pandemic attractor. There are many ways we can measure the
86 distance from the attractor, but for illustrative purposes, we choose one of the most
87 parsimonious approach: that is, we look at how the susceptible (S) and infected (I)
88 populations change over time and measure the distance on the SI phase plane (Figure
89 2B). In this simple case, the locally estimated scatterplot smoothing (LOESS) fit in-
90 dicates that the distance from the attractor decreases exponentially (linearly on a log
91 scale) on average (Figure 2C). Furthermore, the overall rate of return approximates
92 the intrinsic resilience of the seasonally unforced system (Figure 2C).

93 Alternatively, NPIs can have a lasting impact on the pathogen dynamics; as an
94 example, we consider a scenario in which a 10% reduction in transmission persists
95 even after the NPIs are lifted (Figure 2D–F). In such cases in practice, we can-
96 not know whether the pathogen will return to its original cycle or a different cycle
97 until many years have passed, and we cannot measure the distance to the new un-
98 known attractor that the system might eventually approach. Nonetheless, we can
99 still measure the distance from the pre-pandemic attractor and ask how the distance
100 changes over time (Figure 2E). The LOESS fit suggests that the distance from the
101 pre-pandemic attractor will initially decrease exponentially on average (equivalently,
102 linearly on a log scale) and eventually plateau (Figure 2F). Here, a permanent 10%
103 reduction in transmission rate slows the system, which causes the distance from the
104 pre-pandemic attractor initially to decrease at a slower rate (Figure 2F) than it would
105 have otherwise (Figure 2C) before plateauing at a fixed distance between the two
106 attractors. This example shows that resilience is not necessarily an intrinsic prop-
107 erty of a specific pathogen. Instead, pathogen resilience is a property of a specific
108 attractor that a host-pathogen system approaches, which depends on both pathogen
109 and host characteristics.

110 Finally, transient phenomena can further complicate the picture (Figure 2G–I).
111 For example, a stage-structured model initially exhibits a stable annual cycle, but
112 perturbations from a 10% reduction in transmission for 6 months cause the epidemic
113 to shift to biennial cycles (Figure 2G). The system eventually approaches the original
114 pre-pandemic attractor (Figure 2H), suggesting that this biennial cycle is a transient
115 phenomenon. The LOESS fit indicates that the distance from the attractor initially

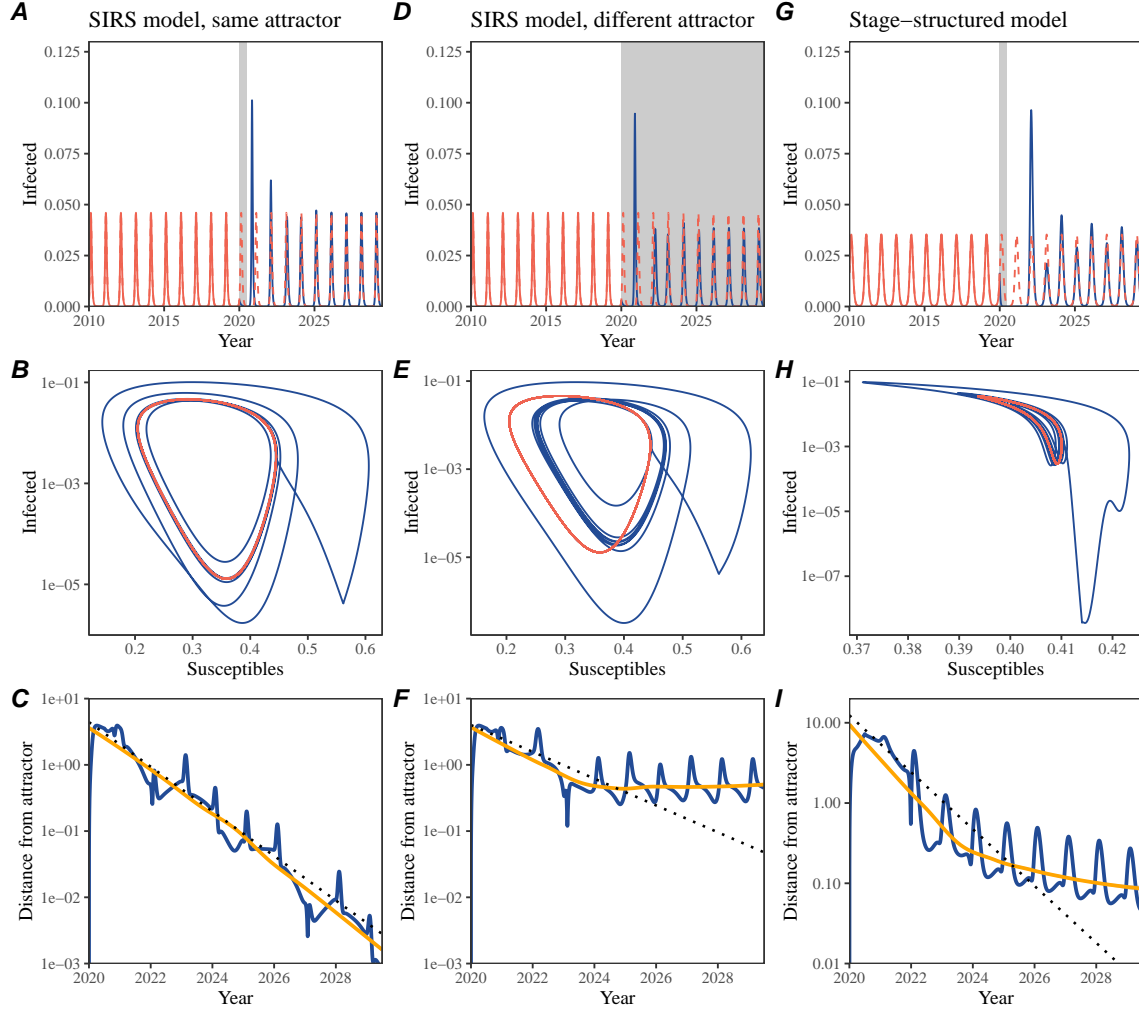


Figure 2: A simple method to measure pathogen resilience following NPIs across different scenarios. (A, D, G) Simulated epidemic trajectories across various models. Red and blue solid lines represent epidemic dynamics before and after interventions are introduced, respectively. Red dashed lines represent counterfactual epidemic dynamics in the absence of interventions. Gray regions indicate the duration of interventions. (B, E, H) Phase plane representation of the time series in panels A, D, and G alongside the corresponding susceptible host dynamics. Red and blue solid lines represent epidemic trajectories on an SI phase plane before and after interventions are introduced, respectively. (C, F, I) Changes in logged distance from the attractor over time. Blue lines represent the logged distance from the attractor. Orange lines represent the locally estimated scatterplot smoothing (LOESS) fits to the logged distance from the attractor. Dotted lines show the intrinsic resilience of the seasonally unforced system.

116 decreases exponentially at a rate that is consistent with the intrinsic resilience of

117 the seasonally unforced stage-structured system, but the rate of decrease decelerates
118 with the damped oscillations (Figure 2I). This behavior is also referred to as a ghost
119 attractor, which causes long transient dynamics and slow transitions [16]. Strong
120 seasonal forcing in transmission can also lead to transient phenomena for a simple
121 SIRS model, causing a slow return to pre-perturbation dynamics (Supplementary
122 Figure S1).

123 This empirical approach allows us to measure the resilience of a two-strain host-
124 pathogen system even when we have incomplete observation of the infection dynam-
125 ics. Simulations from a simple two-strain system illustrate that separate analyses of
126 individual strain dynamics (e.g., RSV A vs B) and a joint analysis of total infections
127 (e.g., total RSV infections) yield identical resilience estimates (Supplementary Fig-
128 ure S2, 3). This is expected because the dynamics of two strains (or two pathogens)
129 around the attractor in a coupled system are described by the same set of eigen-
130 values and eigenvectors, meaning that both strains should exhibit identical rates of
131 returns following a perturbation. Analogous to a single system, strong seasonal forc-
132 ing in transmission can cause the system to slow down through transient phenomena
133 (Supplementary Figure S4).

134 These observations indicate three possibilities. First, we can directly estimate the
135 empirical resilience of a host-pathogen system by measuring the rate at which the
136 system approaches an attractor, provided that we have a way to quantify the distance
137 from the attractor. The empirical approach to estimating pathogen resilience is
138 particularly convenient because it does not require us to know the true underlying
139 model; estimating the intrinsic resilience from fitting misspecified models can lead
140 to biased estimates (Supplementary Figure S5). Second, resilience estimates allow
141 us to make phenomenological predictions about the dynamics of a host-pathogen
142 system following a perturbation. Assuming that the distance from the attractor will
143 decrease exponentially over time, we can obtain a ballpark estimate for when the
144 system will reach an attractor; this prediction necessarily assumes that there won't
145 be permanent changes in pathogen dynamics (Figure 2F) or a long-term transient
146 phenomenon (Figure 2I). Finally, a change in the rate of an exponential decrease in
147 the distance from the attractor can provide information about whether the system
148 has reached an alternative attractor, or a ghost attractor, that is different from the
149 original, pre-pandemic attractor. These alternative attractors may reflect continued
150 perturbations from permanent changes in transmission patterns as well as changes in
151 immune landscapes. There will be periods of time when it is difficult to tell whether
152 pathogen dynamics are still diverging from its original attractor or have begun to
153 converge to an attractor; now that several years have passed since NPIs have been
154 lifted, we expect many respiratory pathogens to have had sufficient time to begin
155 returning to their post-NPI attractors.

156 **Inferring pathogen resilience from real data**

157 Based on these observations, we now lay out our approach to estimating pathogen
158 resilience from real data (Figure 3). We then test this approach against simulations
159 and apply it to real data.

160 So far, we focused on simple examples that assume a constant transmission re-
161 duction. However, in practice, the impact of NPIs on pathogen transmission is likely
162 more complex (Figure 3A), reflecting introduction and relaxation of various NPI
163 strategies. In some cases, strong NPIs can even lead to a local fadeout, requiring im-
164 migration from another location for epidemic re-emergence. These complexities can
165 lead to longer delays between the introduction of NPIs and pathogen re-emergence as
166 well as temporal variation in outbreak sizes (Figure 3B): in this example, continued
167 transmission reduction from NPIs limits the size of the first outbreak in 2021 fol-
168 lowing the emergence, allowing for a larger outbreak in 2022 when NPIs are further
169 relaxed.

170 Previously, we relied on the dynamics of susceptible and infected hosts to com-
171 pute the distance from the attractor (Figure 2), but information on susceptible hosts
172 is rarely available in practice. In addition, uncertainties in case counts due to obser-
173 vation error as well as multiannual cycles in the observed epidemic dynamics (e.g.,
174 adenovirus circulation patterns in Hong Kong and Korea) add challenges to defining
175 pre-pandemic attractors, which limits our ability to measure the distance from
176 the attractor. To address these challenges, we can reconstruct an empirical attrac-
177 tor by utilizing Takens' theorem [14], which states that an attractor of a nonlinear
178 multidimensional system can be mapped onto a delayed embedding (Materials and
179 Methods). For example, we can use delayed logged values of pre-pandemic cases $C(t)$
180 (Figure 3C) to reconstruct the attractor:

$$\langle \log(C(t) + 1), \log(C(t - \tau) + 1), \dots, \log(C(t - (M - 1)\tau) + 1) \rangle, \quad (1)$$

181 where the delay τ and embedding dimension M are determined based on autocor-
182 relations and false nearest neighbors, respectively [17, 18]. We can then apply the
183 same delay and embedding dimensions to the entire time series to determine the
184 position on a multi-dimensional state space (Figure 3D), which allows us to mea-
185 sure the nearest neighbor distance between the current state of the system and the
186 empirical pre-pandemic attractor (Figure 3E). In theory, we can now quantify how
187 fast this distance decreases by fitting a linear regression on a log scale, where the
188 slope of the linear regression corresponds to pathogen resilience. However, resulting
189 estimates of pathogen resilience can be sensitive to choices about embedding delays
190 and dimensions; for example, using longer delays and higher dimensions tends to
191 smooth out temporal variations in the distance from the attractor (Supplementary
192 Figure S6).

193 Complex changes in the distance from the attractor suggest that estimating
194 pathogen resilience from linear regression will be particularly sensitive to our choice
195 of fitting windows for the regression (Figure 3E). Therefore, before we tried estimat-

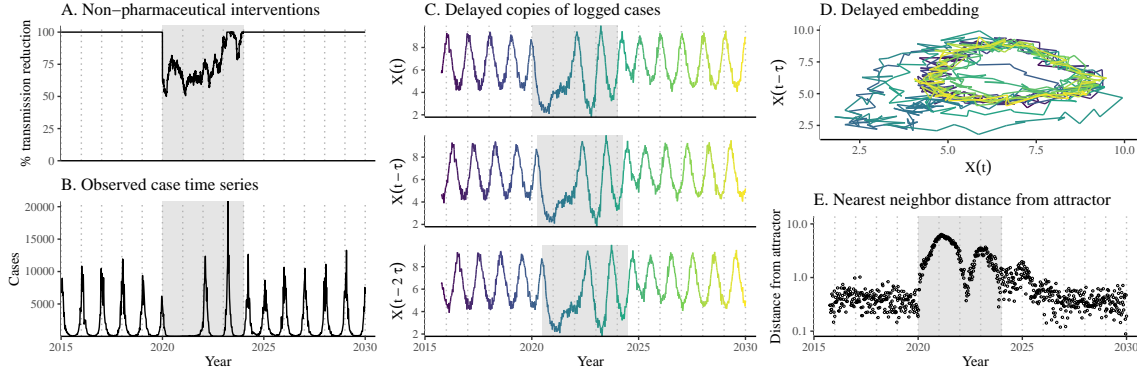


Figure 3: **A schematic diagram explaining the inference of pathogen resilience from synthetic data.** (A) A realistic example of simulated NPIs, represented by a relative reduction in transmission. (B) The impact of the synthetic NPI on epidemic dynamics simulated using a SIRS model with demographic stochasticity. (C) Generating delayed copies of the logged time series allows us to obtain an embedding. (D) Two dimensional representation of an embedding. (E) Delayed embedding allows us to calculate the nearest neighbor distance from the empirical attractor, which is determined based on the pre-pandemic time series. This distance time series can be used to infer pathogen resilience after choosing an appropriate window for linear regression.

ing resilience from real data, we explored an automated window selection criterion for linear regression and test it against randomized, stochastic simulations across a wide range of realistic NPI shape; in doing so, we also explored optimal choices for embedding dimensions and evaluated our choices for fitting window parameters and embedding dimensions by quantifying correlation coefficients between the estimated resilience and the intrinsic resilience of a seasonally unforced system (Materials and Methods). Overall, we find large variation in estimation performances with correlation coefficient ranging from 0.21 to 0.61 (Supplementary Figure S7). In almost all cases, the automated window selection approach outperformed a naive approach that uses the entire time series, starting from the peak distance (Supplementary Figure S7).

Based on the best performing window selection criteria and embedding dimension, we applied this approach to pathogen surveillance data presented in Figure 1 (Materials and Methods). For each time series, we applied Takens' theorem independently to reconstruct the empirical attractor and obtained the corresponding time series of distances from attractors (Supplementary Figure S8). Then, we use the automated window selection criterion to fit a linear regression and estimate the empirical resilience for each pathogen in each country (Supplementary Figure S8); the window selection criterion gave poor regression window for three cases (norovirus in Hong Kong and Korea and Rhinovirus/Enterovirus in the US), leading to unrealistically low resilience estimates, and so we used ad-hoc regression windows instead

217 (Supplementary Figure S9; Materials and Methods).

218 For all pathogens we consider, resilience estimates fall between 0.4/year and
219 1.8/year (Figure 4A). We estimate the mean resilience of common respiratory pathogens
220 to be 0.99/year (95% CI: 0.80/year–1.18/year). As a reference, this is \approx 7.5 times
221 higher than the intrinsic resilience of pre-vaccination measles in England and Wales
222 (\approx 0.13/year). Finally, resilience estimates for norovirus are comparable to those of
223 common respiratory pathogens: 1.44/year (95%CI: 1.01/year–1.87/year) for Hong
224 Kong and 1.07/year (95%CI: 0.86/year–1.29/year) for Korea. Based on a simple
225 ANOVA test, we do not find significant differences in resilience estimates across
226 countries ($p = 0.25$) or pathogens ($p = 0.68$).

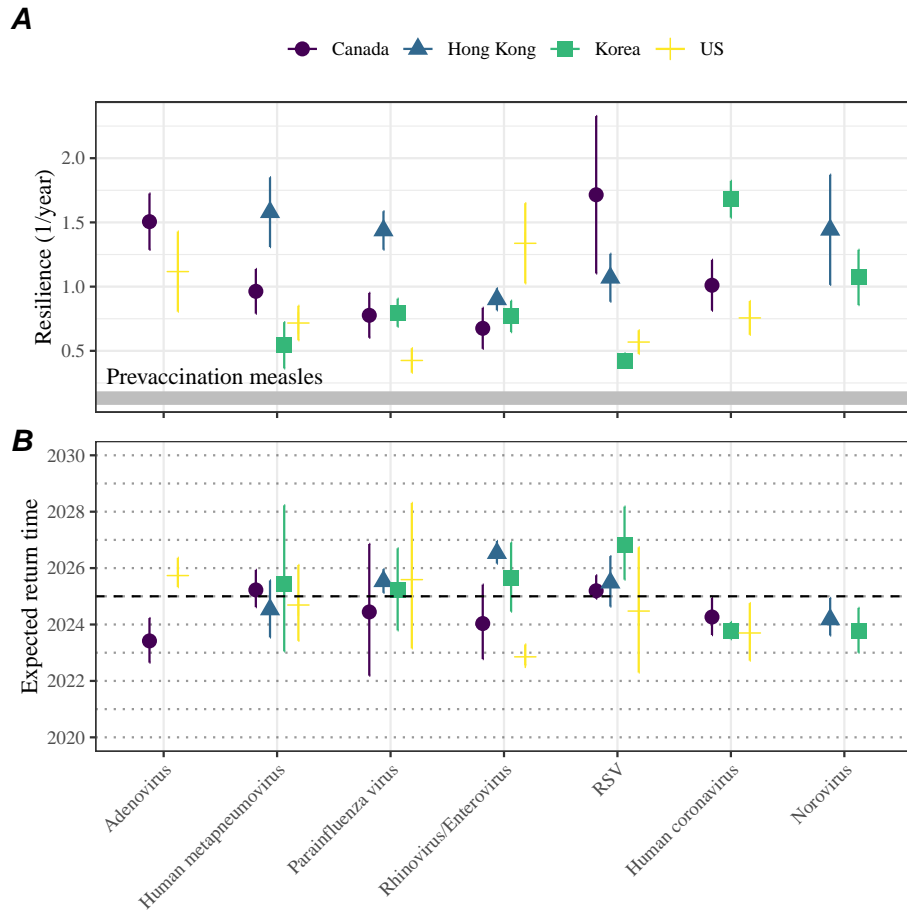


Figure 4: **Summary of resilience estimates.** (A) Estimated pathogen resilience. The gray horizontal line represents the intrinsic resilience of pre-vaccination measles dynamics. (B) Predicted timing of when each pathogen will return to their pre-pandemic cycles. The dashed line in panel B indicates the end of 2024 (current observation time). Error bars represent 95% confidence intervals.

227 [SWP: You suggested “I think we probably need to spell out a bit more that

228 long-term changes in the transmission rate (or some other parameter) mean the at-
229 tractor is permanently different and the distance should remain nonzero” and I think
230 we’ve done that enough early on with current revisions so I don’t feel like we need
231 to do it again here. Let me know what you think.] Using resilience estimates, we
232 now predict when each pathogen would hypothetically return to their pre-pandemic
233 dynamics, assuming no long-term change in the attractor. Specifically, we extend
234 our linear regression fits to distance-from-attractor time series and ask when the pre-
235 dicted regression line will cross a threshold value; since we relied on nearest neighbor
236 distances, pre-pandemic distances are always greater than zero (Figure 3E), meaning
237 that we can use the mean of pre-pandemic distances as our threshold. We predict
238 that a return to pre-pandemic cycles would be imminent for most pathogens (Figure
239 4B). We also predict that many pathogens should have already returned to their pre-
240 pandemic dynamics by the end of 2024, but these predictions contradict some of the
241 observed pathogen dynamics. For example, we predict that both human metapneu-
242 movirus and RSV in Korea should have returned to their attractors by now, but the
243 magnitude and timing of recent epidemics are different from pre-pandemic patterns
244 (Figure 1). These observations suggest the possibility that some common respiratory
245 pathogens may have converged to different attractors.

246 In Supplementary Materials, we also consider using a lower threshold for the false
247 nearest neighbor approach when determining the embedding dimension; this gives a
248 higher embedding dimension. As explained earlier (Supplementary Figure S6), this
249 gives a smoother distance-from-attractor time series (compare Supplementary Figure
250 S10 with S8); this also requires us to use longer time series, which prevents us from
251 estimating resilience for some pathogens. Overall, resulting estimates of pathogen
252 resilience with higher embedding dimensions still mostly fall between 0.3/year and
253 2.1/year (Supplementary Figure S11). A direct comparison between two approaches
254 (i.e., original estimate vs using higher dimensions) shows a strong consistency in
255 resilience estimates (Supplementary Figure S12).

256 Susceptible host dynamics explain variation in pathogen 257 resilience

258 So far, we focused on quantifying pathogen resilience from the observed patterns of
259 pathogen re-emergence following NPIs. But what factors determine how resilient a
260 host-pathogen system is? Here, we use the SIRS model to show that susceptible host
261 dynamics are the key determinants of pathogen resilience. To do so, we vary the
262 basic reproduction number \mathcal{R}_0 , which represents the average number of secondary
263 infections caused by a newly infected individual in a fully susceptible population,
264 and the duration of immunity and compute intrinsic resilience for each parameter.

265 We find an increase in \mathcal{R}_0 and a decrease in duration of immunity correspond
266 to an increase in pathogen resilience (Figure 5A). These variations can be under-
267 stood in terms of the susceptible host dynamics, where faster per-capita susceptible

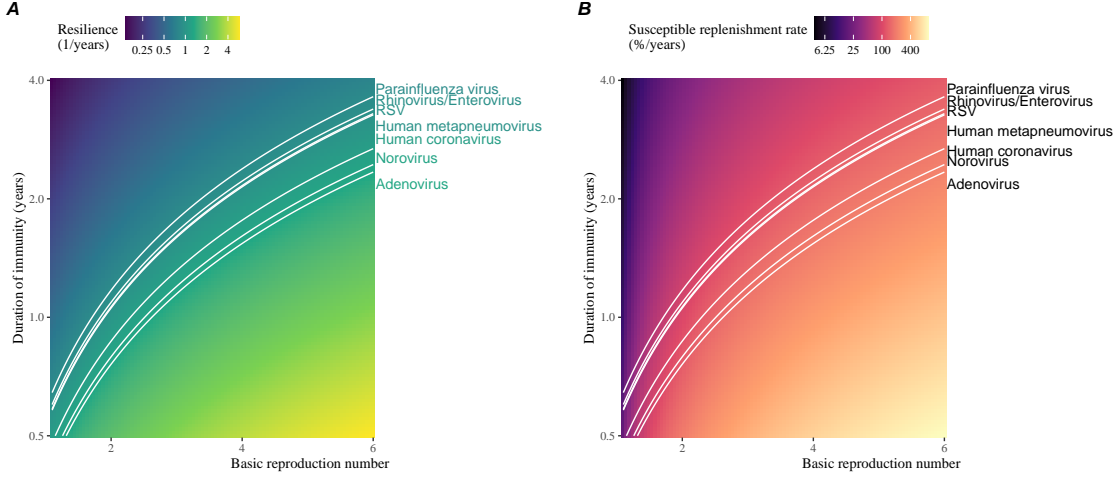


Figure 5: Linking pathogen resilience to epidemiological parameters and susceptible host dynamics. (A) The heat map represents intrinsic resilience as a function of the basic reproduction number \mathcal{R}_0 and the duration of immunity. (B) The heat map represents per-capita susceptible replenishment rate as a function of the basic reproduction number \mathcal{R}_0 and the duration of immunity. The standard SIRS model is used to compute intrinsic resilience and per-capita susceptible replenishment rate. Lines correspond to a set of parameters that are consistent with mean resilience estimates for each pathogen. Pathogens are ranked based on their mean resilience estimates, averaged across different countries.

replenishment rate causes the system to be more resilient (Figure 5B). This rate can be expressed as a ratio between absolute rate at which new susceptibles enter the population and the equilibrium number of susceptible individuals in the population, \bar{S} . Therefore, both higher \mathcal{R}_0 and shorter duration of immunity can drive faster per-capita susceptible replenishment rate (Figure 5B), especially because higher \mathcal{R}_0 leads to lower \bar{S} .

Finally, we can rank different pathogens based on the average values of empirical resilience computed previously, which allows us to determine a set of parameters that are consistent with the estimated resilience (Figure 5A). Across all pathogens we consider, except for bocavirus and norovirus, we estimate that the average duration of immunity is likely to be short (< 6 years) across a plausible range of \mathcal{R}_0 . These rankings further allow us to map each pathogen onto a set of SIRS parameters that are consistent with its empirical resilience (Figure 5A) and obtain a plausible range of susceptible replenishment rates for each pathogen (Figure 5B). However, we note that there is no one-to-one correspondence between susceptible replenishment rates and pathogen resilience, leading to a wide uncertainty in the estimates for susceptible replenishment rates (Figure 5B).

285 **Discussion**

286 The pandemic NPIs have caused major disruptions to circulation patterns of both
287 respiratory and non-respiratory pathogens, adding challenges to predicting their fu-
288 ture dynamics [1, 2, 3, 4]. However, these NPIs offer large-scale natural experiments
289 for understanding how different pathogens respond to perturbations. In this study,
290 we show that pathogen re-emergence patterns following NPIs can be characterized
291 through the lens of ecological resilience. Traditionally, ecological resilience measures
292 how fast a system returns to a reference state following a perturbation. In the con-
293 text of respiratory pathogens, resilience measures how fast epidemics return to their
294 endemic cycles after NPIs are lifted.

295 We use an attractor reconstruction approach to quantify how distance from the
296 attractor changes over time for each pathogen [14]. We show that the resilience of
297 a host-pathogen system can be estimated by fitting a linear regression to a logged
298 distance-from-attractor time series. Overall, we estimate that the resilience for most
299 common respiratory pathogens ranges between 0.4/year and 1.8/year, which is 3–14
300 times more resilient than prevaccination measles, indicating potential challenges in
301 controlling common respiratory pathogens.

302 Our framework allows us to make phenomenological predictions about when each
303 pathogen will return to their endemic cycles. The ability to predict future epidemic
304 patterns from resilience estimates offers a new paradigm for epidemic forecasting.
305 While this approach cannot predict the exact timing of outbreaks or epidemic pat-
306 terns, it is nonetheless useful for predicting when epidemics will settle down to regular
307 cycles after a large perturbation, such as pandemic NPIs.

308 Our analyses suggest a possibility that several pathogens may have converged
309 to different endemic cycles compared to their pre-pandemic epidemic patterns. Key
310 examples include human metapnuemovirus, RSV, and bocavirus in Korea as well as
311 RSV in Hong Kong. These changes may reflect changes in surveillance or actual shift
312 in the dynamics, caused by permanent changes in behavior or population-level immu-
313 nity. While it seems unlikely that permanent changes in behavior would only affect a
314 few pathogens and not others, we cannot rule out this possibility given heterogeneity
315 in the age of infection across different respiratory pathogens [SWP: CITE]. A shift
316 in population-level immunity is plausible, as the emergence of SARS-CoV-2 and ex-
317 tinction of influenza B/Yamagata likely caused major changes in immune landscapes;
318 interactions among co-circulating pathogens, such as cross immunity between RSV
319 and HMPV [19], may have also contributed to changes in population-level immu-
320 nity. However, we currently do not know how immunity, or lack thereof, from these
321 pathogens would affect infection from other pathogens. Future studies should use
322 detailed mechanistic models, coupled with behavioral and immunological data, to
323 test these hypotheses and better understand post-pandemic dynamics of endemic
324 pathogens.

325 We show that susceptible host dynamics shape pathogen resilience, where faster
326 replenishment of the susceptible population causes the pathogen to be more resilient.

327 For simplicity, we focus on waning immunity and birth as the main drivers of the
328 susceptible host dynamics but other mechanisms can also contribute to the replen-
329 ishment of the susceptible population. In particular, pathogen evolution, especially
330 the emergence of antigenically novel strains, can cause effective waning of immunity
331 in the population; therefore, we hypothesize that faster rates of antigenic evolution
332 can also cause a pathogen to be more resilient. Future studies should explore the
333 relationship between the rate of evolution and resilience for antigenically evolving
334 pathogens.

335 Quantifying pathogen resilience also offers novel approaches to validating population-
336 level epidemiological models. So far, most of model validation in infectious disease
337 ecology is based on the ability of a model to reproduce the observed epidemic dy-
338 namics and to predict future dynamics [20, 19, 21, 22, 23]. However, many models
339 can perform similarly under these criteria. For example, two major RSV models
340 have been proposed to explain biennial epidemic patterns: (1) a stage- and age-
341 structured model that allows disease severity to vary with number of past infections
342 and age of infection [21] and (2) a pathogen-interaction model that accounts for cross
343 immunity between RSV and human metapneumovirus [19]. Since both models can
344 accurately reproduce the observed epidemic patterns, standard criteria for model
345 validation do not allow us to distinguish between these two models from population-
346 level data alone. Instead, it would be possible to measure the empirical resilience of
347 each model by simulating various perturbations and compare them to estimates of
348 empirical resilience from data, using pandemic NPIs as an opportunity.

349 There are several limitations to our work. First, we did not extensively explore
350 other approaches to reconstructing the attractor. Recent studies showed that more
351 sophisticated approaches, such as using non-uniform embedding, can provide more
352 robust reconstruction for noisy data [18]. In the context of causal inference, choices
353 about embedding can have major impact on the resulting inference [24]. Our re-
354 silience estimates are likely overly confident given a lack of uncertainties in attractor
355 reconstruction as well as the simplicity of our statistical framework. Short pre-
356 pandemic time series also contribute to the crudeness of our estimates. Nonetheless,
357 as illustrated in our sensitivity analyses (Supplementary Figure S6, S10–S12), infer-
358 ences about pathogen resilience in our SIRS model appear to be robust to decisions
359 about embedding lags and dimensions—this is because tracking the rate at which
360 the system approaches the attractor is likely a much simpler problem than making
361 inferences about causal directionality. Our qualitative prediction that common res-
362 piratory pathogens are more resilient than prevaccination measles is also likely to be
363 robust to these predictions, given how rapid many respiratory pathogens returned to
364 their original cycles following pandemic NPIs.

365 Predicting the impact of anthropogenic changes on infectious disease dynamics
366 is a fundamental aim of infectious disease research in a rapidly changing world. Our
367 study illustrates that quantifying pathogen resilience can help us understand how
368 infectious disease pathogens respond to major perturbations caused by NPIs. More
369 broadly, a detailed understanding of the determinants of pathogen resilience may

370 offer unique insights into pathogen persistence and controllability.

371 Materials and Methods

372 Data

373 We gathered time series on respiratory infections from Canada, Hong Kong, Korea,
374 and United States (US). As a reference, we also included time series data on norovirus
375 infections for available countries—in contrast to respiratory pathogens, we expect
376 gastrointestinal viruses, such as norovirus, to be differently affected by pandemic
377 NPIs. For all time series, we rounded every year to 52 weeks by taking the average
378 number of cases and tests between the 52nd and 53rd week. We also rescale all time
379 series to account for changes in testing patterns, which are then used for the actual
380 analysis.

381 Weekly time series of respiratory infection cases in Canada comes from the Res-
382piratory Virus Detection Surveillance System, which collect data from select labo-
383ratories across Canada. We extracted the data from <https://www.canada.ca/en/public-health/services/surveillance/respiratory-virus-detections-canada.html>. To account for an increase in testing from 2013 to 2024, we calculate a 2 year
385 moving average for the number of tests for each pathogen, which we use as a proxy
386 for testing effort. Then, we divide the smoothed testing patterns by the smoothed
387 value at the final week such that the testing effort has a maximum of 1. We then
388 divide weekly cases by the testing effort to obtain a scaled case time series. A similar
389 approach was used earlier for the analysis of RSV time series in the US [21].

391 Weekly time series of respiratory infection cases in Hong Kong comes from the
392 Centre for Health Protection, Department of Health. We extract the data from
393 <https://www.chp.gov.hk/en/statistics/data/10/641/642/2274.html>. We also
394 apply the same scaling procedure to the time series as we did for Canada. For Hong
395 Kong, we only adjust for testing efforts up to the end of 2019 because there was a
396 major reduction in testing for common respiratory pathogens since 2020.

397 Weekly time series of acute respiratory infection cases in Korea comes from Ko-
398rea Disease Control and Prevention Agency. We extract the data from <https://dportal.kdca.go.kr/pot/is/st/ari.do>. While we do not have information on
399 testing, the reported number of respiratory infections consistently increased from
400 2013 to the end of 2019, which we interpreted as changes in testing patterns. Since
401 we do not have testing numbers, we used the weekly sum of all acute respiratory vi-
402ral infection cases as a proxy for testing, which were further smoothed with moving
403 averaged and scaled to have a maximum of 1. For Korea, we also only adjust for
404 testing efforts up to the end of 2019.

406 Finally, weekly time series of respiratory infection cases in the US comes from
407 the National Respiratory and Enteric Virus Surveillance System. In the US, there
408 has been a large increase in testing against some respiratory pathogens, especially
409 RSV, which could not be corrected for through simple scaling. Instead, we derive an

410 incidence proxy by multiplying the test positivity with influenza-like illness positivity,
 411 which is taken from <https://gis.cdc.gov/grasp/fluvview/fluportaldashboard.html>.
 412 This method of estimating an incidence proxy has been recently applied in
 413 the analysis of seasonal coronaviruses [7] and *Mycoplasma pneumoniae* infections [4].
 414 Detailed assumptions and justifications are provided in [25].

415 **Estimating pathogen resilience**

416 In order to measure pathogen resilience from surveillance data, we first reconstruct
 417 the empirical pre-pandemic attractor of the system using Takens' embedding theorem
 418 [14]. Specifically, for a given pathogen, we take the pre-pandemic (before 2020)
 419 case time series $C(t)$ and reconstruct the attractor using delayed embedding with a
 420 uniform delay of τ and dimension M :

$$X_{\tau,m}(t) = \langle \log(C(t) + 1), \log(C(t - \tau) + 1), \dots, \log(C(t - (M - 1)\tau) + 1) \rangle. \quad (2)$$

421 Here, the delay τ is determined by calculating the autocorrelation of the logged pre-
 422 pandemic time series and asking when the autocorrelation crosses 0 for the first time
 423 [18]; a typical delay for an annual outbreak is around 13 weeks.

424 Then, for a given delay τ , we determine the embedding dimension M using the
 425 false nearest neighbors approach [17, 18]. To do so, we start with an embedding
 426 dimension e and construct a set of points $A_{\tau,e} = \{X_{\tau,e}(t) | t < 2020\}$. Then, for
 427 each point $X_{\tau,e}(t)$, we determine the nearest neighbor from the set $A_{\tau,e}$, which we
 428 denote $X_{\tau,e}(t_{nn})$ for $t \neq t_{nn}$. Then, if the distance between these two points on
 429 $e + 1$ dimension, $D_{\tau,e+1}(t) = \|X_{\tau,e+1}(t_{nn}) - X_{\tau,e+1}(t)\|_2$, is larger than their distance
 430 on e dimension, $D_{\tau,e}(t) = \|X_{\tau,e}(t_{nn}) - X_{\tau,e}(t)\|_2$, these two points are deemed to
 431 be false nearest neighbors; specifically, we use a threshold R for the ratio between
 432 two distances $D_{\tau,e+1}(t)/D_{\tau,e}(t)$ to determine false nearest neighbors. In the main
 433 text, we determine the embedding dimension based on the first dimension without
 434 any false nearest neighbors for $R = 10$. In Supplementary Materials, we impose
 435 $R = 5$ to select for higher dimensions. Once we determine the embedding lag τ
 436 and dimension M , we apply the embedding to the entire time series and calculate
 437 the nearest neighbor distance against the attractor $A_{\tau,M}$ to obtain a time series of
 438 distance from the attractor $D_{\tau,M}(t)$.

439 From a time series of distances from the attractor, we estimate pathogen resilience
 440 by fitting a linear regression to an appropriate window. To automatically select
 441 the fitting window, we begin by smoothing the distance time series using locally
 442 estimated scatterplot smoothing (LOESS) to obtain $\hat{D}_{\tau,M}(t)$, where the smoothing
 443 is performed on a log scale and exponentiated afterwards. Then, we determine
 444 threshold values (T_{start} and T_{end}) for the smoothed distances and choose the fitting
 445 window based on when $\hat{D}_{\tau,M}(t)$ crosses these threshold values for the first time.
 446 These thresholds are determined by first calculating maximum distance,

$$\max \hat{D} = \max \hat{D}_{\tau,M}(t), \quad (3)$$

⁴⁴⁷ and mean pre-pandemic distance,

$$\hat{D}_{\text{mean}} = \frac{1}{N_{t<2020}} \sum_{t<2020} \hat{D}_{\tau,M}(t), \quad (4)$$

⁴⁴⁸ as a reference, and then dividing their ratios into 10 equal bins:

$$T_{\text{start}} = \hat{D}_{\text{mean}} \times \left(\frac{\max \hat{D}}{\hat{D}_{\text{mean}}} \right)^{9/10} \quad (5)$$

$$T_{\text{end}} = \hat{D}_{\text{mean}} \times \left(\frac{\max \hat{D}}{\hat{D}_{\text{mean}}} \right)^{1/10} \quad (6)$$

⁴⁴⁹ This allows us to discard the initial period during which the distance increases (from
⁴⁵⁰ the introduction of intervention measures) and the final period during which the
⁴⁵¹ distance plateaus (as the system reaches an attractor). The fitting window is deter-
⁴⁵² mined based on when the smoothed distance $\hat{D}_{\tau,M}(t)$ crosses these threshold values
⁴⁵³ for the first time; then, we fit a linear regression to logged (unsmoothed) distances
⁴⁵⁴ $\log D_{\tau,M}(t)$ using that window.

⁴⁵⁵ Mathematical modeling

⁴⁵⁶ Throughout the paper, we use a series of mathematical models to illustrate the con-
⁴⁵⁷ cept of pathogen resilience and to understand the determinants of pathogen resilience.
⁴⁵⁸ In general, the intrinsic resilience for a given system is given by the largest real part
⁴⁵⁹ of the eigenvalues of the linearized system at endemic equilibrium. Here, we focus on
⁴⁶⁰ the SIRS model with demography and present the details of other models in Supple-
⁴⁶¹ mentary Materials. The SIRS (Susceptible-Infected-Recovered-Susceptible) model is
⁴⁶² the simplest model that allows for waning of immunity, where recovered (immune)
⁴⁶³ individuals are assumed to become fully susceptible after an average of $1/\delta$ time pe-
⁴⁶⁴ riod. The dynamics of the SIRS model is described by the following set of differential
⁴⁶⁵ equations:

$$\frac{dS}{dt} = \mu - \beta(t)SI - \mu S + \delta R \quad (7)$$

$$\frac{dI}{dt} = \beta(t)SI - (\gamma + \mu)I \quad (8)$$

$$\frac{dR}{dt} = \gamma I - (\delta + \mu)R \quad (9)$$

$$(10)$$

⁴⁶⁶ where μ represents the birth/death rate, $\beta(t)$ represents the time-varying trans-
⁴⁶⁷ mission rate, and γ represents the recovery rate. The basic reproduction number
⁴⁶⁸ $\mathcal{R}_0(t) = \beta(t)/(\gamma + \mu)$ is defined as the average number of secondary infections that

469 a single infected individual would cause in a fully susceptible population at time t
 470 and measures the intrinsic transmissibility of a pathogen.

471 When we first introduce the idea of pathogen resilience (Figure 2), we impose
 472 sinusoidal changes to the transmission rate to account for seasonal transmission:

$$\beta(t) = b_1(1 + \theta \cos(2\pi(t - \phi)))\alpha(t), \quad (11)$$

473 where b_1 represents the baseline transmission rate, θ represents the seasonal am-
 474 plitude, and ϕ represents the seasonal offset term. Here, we also introduce an ex-
 475 tra multiplicative term $\alpha(t)$ to account for the impact of pandemic NPIs, where
 476 $\alpha(t) < 1$ indicates transmission reduction. Figure 2A and 2B are generated assum-
 477 ing $b_1 = 3 \times (365/7 + 1/50)/\text{years}$, $\theta = 0.2$, $\phi = 0$, $\mu = 1/50/\text{years}$, $\gamma = 365/7/\text{years}$,
 478 and $\delta = 1/2/\text{years}$. In Figure 2A, we impose a 50% transmission reduction for 6
 479 months from 2020:

$$\alpha(t) = \begin{cases} 0.5 & 2020 \leq t < 2020.5 \\ 1 & \text{otherwise} \end{cases} \quad (12)$$

480 In Figure 2B, we impose a 50% transmission reduction for 6 months from 2020 and
 481 a permanent 10% reduction onward:

$$\alpha(t) = \begin{cases} 1 & t < 2020 \\ 0.5 & 2020 \leq t < 2020.5 \\ 0.9 & 2020.5 \leq t \end{cases} \quad (13)$$

482 In both scenarios, we simulate the SIRS model from the following initial conditions
 483 ($S(0) = 1/\mathcal{R}_0$, $I(0) = 1 \times 10^{-6}$, and $R(0) = 1 - S(0) - I(0)$) from 1900 until 2030.

484 To measure the empirical resilience of the SIR model (Figure 2C and 2F), we
 485 compute the normalized distance between post-intervention susceptible and logged
 486 infected proportions and their corresponding pre-intervention values at the same time
 487 of year:

$$\sqrt{\left(\frac{S(t) - S_{\text{pre}}(t)}{\sigma_S}\right)^2 + \left(\frac{\log I(t) - \log I_{\text{pre}}(t)}{\sigma_{\log I}}\right)^2}, \quad (14)$$

488 where σ_S and $\sigma_{\log I}$ represent the standard deviation in the pre-intervention suscep-
 489 tible and logged infected proportions. We normalize the differences in susceptible
 490 and logged infected proportions to allow both quantities to equally contribute to the
 491 changes in distance from the attractor. We used logged prevalence, instead of abso-
 492 lute prevalence, in order to capture epidemic dynamics in deep troughs during the
 493 intervention period. In Supplementary Materials, we also compare how the degree
 494 of seasonal transmission affects empirical resilience by varying θ from 0 to 0.4; when
 495 we assume no seasonality ($\theta = 0$), we do not normalize the distance because the
 496 standard deviation of pre-intervention dynamics are zero.

497 Finally, we use the SIRS model to understand how underlying epidemiological
 498 parameters affect pathogen resilience and link this relationship to underlying sus-
 499 ceptible host dynamics. For the simple SIRS model without seasonal transmission

500 $(\theta = 0)$, the intrinsic resilience corresponds to

$$-\frac{\text{Re}(\lambda)}{2} = \frac{\delta + \beta I^* + \mu}{2}. \quad (15)$$

501 Here, I^* represents the prevalence at endemic equilibrium:

$$I^* = \frac{(\delta + \mu)(\beta - (\gamma + \mu))}{\beta(\delta + \gamma + \mu)}. \quad (16)$$

502 The susceptible replenishment rate is given by

$$S_{\text{replenish}} = \frac{\mu + \delta R}{S^*}, \quad (17)$$

503 where $S^* = 1/\mathcal{R}_0$ represents the equilibrium proportion of susceptible individuals.
504 We vary the basic reproduction number \mathcal{R}_0 between 1.1 to 6 and the average duration
505 of immunity $1/\delta$ between 2 to 80 years, and compute these two quantities. In doing
506 so, we fix all other parameters: $\mu = 1/80/\text{years}$ and $\gamma = 365/7/\text{years}$.

507 Data availability

508 Funding

509 **Supplementary Text**

510 **Resilience of a stage-structured system.**

511 In Figure 2G–I, we use a more realistic, stage-structured model to illustrate how
 512 transient phenomena can cause the system to slow down. Specifically, we use the
 513 stage-structured RSV model proposed by [21], which assumes that subsequent rein-
 514 fections cause an individual to become less susceptible and transmissible than previ-
 515 ous infections. The model dynamics can be described as follows:

$$\frac{dM}{dt} = \mu - (\omega + \mu)M \quad (S1)$$

$$\frac{dS_0}{dt} = \omega M - (\lambda(t) + \mu)S_0 \quad (S2)$$

$$\frac{dI_1}{dt} = \lambda(t)S_0 - (\gamma_1 + \mu)I_1 \quad (S3)$$

$$\frac{dS_1}{dt} = \gamma_1 I_1 - (\sigma_1 \lambda(t) + \mu)S_1 \quad (S4)$$

$$\frac{dI_2}{dt} = \sigma_1 \lambda(t)S_1 - (\gamma_2 + \mu)I_2 \quad (S5)$$

$$\frac{dS_2}{dt} = \gamma_2 I_2 - (\sigma_2 \lambda(t) + \mu)S_2 \quad (S6)$$

$$\frac{dI_3}{dt} = \sigma_2 \lambda(t)S_2 - (\gamma_3 + \mu)I_3 \quad (S7)$$

$$\frac{dS_3}{dt} = \gamma_3 I_3 - (\sigma_3 \lambda(t) + \mu)S_3 + \gamma_4 I_4 \quad (S8)$$

$$\frac{dI_4}{dt} = \sigma_3 \lambda(t)S_3 - (\gamma_4 + \mu)I_4 \quad (S9)$$

(S10)

516 where M represents the proportion of individuals who are maternally immune; S_i
 517 represents the proportion of individuals who are susceptible after i prior infections; I_i
 518 represents the proportion of individuals who are currently (re)-infected with their i -th
 519 infection; μ represents the birth and death rates; $1/\omega$ represents the mean duration
 520 of maternal immunity; $1/\gamma_i$ represents the mean duration of infection; $\lambda(t)$ represents
 521 the force of infection; and σ_i represents the reduction in susceptibility for the i -th
 522 reinfection. The force of infection is modeled using a sinusoidal function:

$$\beta(t) = b_1(1 + \theta \cos(2\pi(t - \phi)))\alpha(t) \quad (S11)$$

$$\lambda(t) = \beta(I_1 + \rho_1 I_2 + \rho_2(I_3 + I_4)), \quad (S12)$$

523 where b_1 represents the baseline transmission rate; θ represents the seasonal ampli-
 524 tude; ϕ represents the seasonal offset term; $\alpha(t)$ represents the intervention effect;
 525 and ρ_i represents the impact of immunity on transmission reduction. We use the

526 following parameters to simulate the impact of interventions on epidemic dynam-
 527 ics [21]: $b_1 = 9 \times (365/10 + 1/80)/\text{years}$, $\theta = 0.2$, $\phi = -0.1$, $\omega = 365/112/\text{years}$,
 528 $\gamma_1 = 365/10/\text{years}$, $\gamma_2 = 365/7/\text{years}$, $\gamma_3 = 365/5/\text{years}$, $\sigma_1 = 0.76$, $\sigma_2 = 0.6$,
 529 $\sigma_3 = 0.4$, $\rho_1 = 0.75$, $\rho_2 = 0.51$, and $\mu = 1/80/\text{years}$. We assume a 50% transmission
 530 reduction for 6 months from 2020:

$$\alpha(t) = \begin{cases} 0.5 & 2020 \leq t < 2020.5 \\ 1 & \text{otherwise} \end{cases} \quad (\text{S13})$$

531 The model is simulated from 1900 to 2030 using the following initial conditions:
 532 $M = 0$, $S_0 = 1/\mathcal{R}_0 - I_1$, $I_1 = 1 \times 10^{-6}$, $S_1 = 1 - 1/\mathcal{R}_0$, $I_2 = 0$, $S_2 = 0$, $I_3 = 0$,
 533 $S_3 = 0$, and $I_4 = 0$. For the phase plane analysis (Figure 2H) and distance analysis
 534 (Figure 2I), we rely on the average susceptibility,

$$\bar{S} = S_0 + \sigma_1 S_1 + \sigma_2 S_2 + \sigma_3 S_3, \quad (\text{S14})$$

535 and total prevalence,

$$I_{\text{total}} = I_1 + I_2 + I_3 + I_4. \quad (\text{S15})$$

536 These quantities are used to compute the normalized distance from the attractor, as
 537 described in the main text.

538 Resilience of a multistrain system.

539 We use a simple two-strain model to show that a multistrain host-pathogen system
 540 that is coupled through cross immunity can be described by a single resilience value.
 541 The model dynamics can be described as follows [19]:

$$\frac{dS}{dt} = \mu - \mu S - (\lambda_1 + \lambda_2)S + \rho_1 R_1 + \rho_2 R_2 \quad (\text{S16})$$

$$\frac{dI_1}{dt} = \lambda_1 S - (\gamma_1 + \mu)I_1 \quad (\text{S17})$$

$$\frac{dI_2}{dt} = \lambda_2 S - (\gamma_2 + \mu)I_2 \quad (\text{S18})$$

$$\frac{dR_1}{dt} = \gamma_1 I_1 - \lambda_2 \epsilon_{21} R_1 - \rho_1 R_1 + \rho_2 R - \mu R_1 \quad (\text{S19})$$

$$\frac{dR_2}{dt} = \gamma_2 I_2 - \lambda_1 \epsilon_{12} R_2 - \rho_2 R_2 + \rho_1 R - \mu R_2 \quad (\text{S20})$$

$$\frac{dJ_1}{dt} = \lambda_1 \epsilon_{12} R_2 - (\gamma_1 + \mu)J_1 \quad (\text{S21})$$

$$\frac{dJ_2}{dt} = \lambda_2 \epsilon_{21} R_1 - (\gamma_2 + \mu)J_2 \quad (\text{S22})$$

$$\frac{dR}{dt} = \gamma_1 J_1 + \gamma_2 J_2 - \rho_1 R - \rho_2 R - \mu R \quad (\text{S23})$$

542 where S represents the proportion of individuals who are fully susceptible to infections
 543 by both strains; I_1 represents the proportion of individuals who are infected with strain 1 without prior immunity; I_2 represents the proportion of individuals who are infected with strain 2 without prior immunity; R_1 represents the proportion of individuals who are fully immune against strain 1 and partially susceptible to reinfection by strain 2; R_2 represents the proportion of individuals who are fully immune against strain 2 and partially susceptible to reinfection by strain 1; J_1 represents the proportion of individuals who are infected with strain 1 with prior immunity against strain 2; J_2 represents the proportion of individuals who are infected with strain 2 with prior immunity against strain 1; R represents the proportion of individuals who are immune to infections from both strains; μ represents the birth/death rate; λ_1 and λ_2 represent the force of infection from strains 1 and 2, respectively; ρ_1 and ρ_2 represent the waning immunity rate; γ_1 and γ_2 represent the recovery rate; ϵ_{21} and ϵ_{12} represent the susceptibility to reinfection with strains 2 and 1, respectively, given prior immunity from infection with strains 1 and 2, respectively. The force of infection is modeled as follows:

$$\beta_1 = b_1(1 + \theta_1 \sin(2\pi(t - \phi_1)))\alpha(t) \quad (\text{S24})$$

$$\beta_2 = b_2(1 + \theta_2 \sin(2\pi(t - \phi_2)))\alpha(t) \quad (\text{S25})$$

$$\lambda_1 = \beta_1(I_1 + J_1) \quad (\text{S26})$$

$$\lambda_2 = \beta_2(I_2 + J_2) \quad (\text{S27})$$

558 In Supplementary Figures S2–S4, we assume the following parameters: $b_1 = 2 \times$
 559 $52/\text{years}$, $b_2 = 4 \times 52/\text{years}$, $\phi_1 = \phi_2 = 0$, $\epsilon_{12} = 0.9$, $\epsilon_{21} = 0.5$, $\gamma_1 = \gamma_2 = 52/\text{years}$,
 560 $\rho_1 = \rho_2 = 1/\text{years}$, and $\mu = 1/70/\text{years}$. For all simulations, we assume a 50%
 561 transmission reduction for 6 months from 2020:

$$\alpha(t) = \begin{cases} 0.5 & 2020 \leq t < 2020.5 \\ 1 & \text{otherwise} \end{cases} \quad (\text{S28})$$

562 The seasonal amplitude θ is varied from 0 to 0.4. All simulations were ran from 1900
 563 to 2030 with following initial conditions: $S(0) = 1 - 2 \times 10^{-6}$, $I_1(0) = 1 \times 10^{-6}$,
 564 $I_2(0) = 1 \times 10^{-6}$, $R_1(0) = 0$, $R_2(0) = 0$, $J_1(0) = 0$, $J_2(0) = 0$, and $R(0) = 0$.

565 We consider three scenarios for measuring pathogen resilience: (1) we only have
 566 information about strain 1, (2) we only have information about strain 2, and (3)
 567 we are unable to distinguish between strains. In the first two scenarios (see panels
 568 A–C for strain 1 and panels D–F for strain 2), we consider the dynamics of average
 569 susceptibility for each strain and total prevalence:

$$\bar{S}_1 = S + \epsilon_{12}R_2 \quad (\text{S29})$$

$$\hat{I}_1 = I_1 + J_1 \quad (\text{S30})$$

$$\bar{S}_2 = S + \epsilon_{21}R_1 \quad (\text{S31})$$

$$\hat{I}_2 = I_2 + J_2 \quad (\text{S32})$$

⁵⁷⁰ In the third scenario (panels G–I), we consider the dynamics of total susceptible and
⁵⁷¹ infected populations:

$$\hat{S} = S + R_2 + R_1 \quad (\text{S33})$$

$$\hat{I} = I_1 + J_1 + I_2 + J_2 \quad (\text{S34})$$

⁵⁷² These quantities are used to compute the normalized distance from the attractor, as
⁵⁷³ described in the main text.

⁵⁷⁴ Estimating intrinsic resilience using mechanistic model

⁵⁷⁵ We tested whether we can reliably estimate the intrinsic resilience of a system by fit-
⁵⁷⁶ ting a mechanistic model. Specifically, we simulated case time series from stochastic
⁵⁷⁷ SIRS and two-strain models and fitted a simple, deterministic SIRS model using a
⁵⁷⁸ Bayesian framework.

⁵⁷⁹ We simulated the models in discrete time, incorporating demographic stochastic-
⁵⁸⁰ ity:

$$\beta(t) = \mathcal{R}_0 \left(1 + \theta \cos \left(\frac{2\pi t}{364} \right) \right) \alpha(t)(1 - \exp(-\gamma)) \quad (\text{S35})$$

$$\text{FOI}(t) = \beta(t)I(t - \Delta t)/N \quad (\text{S36})$$

$$B(t) \sim \text{Poisson}(\mu N) \quad (\text{S37})$$

$$\Delta S(t) \sim \text{Binom}(S(t - \Delta t), 1 - \exp(-(\text{FOI}(t) + \mu)\Delta t)) \quad (\text{S38})$$

$$N_{SI}(t) \sim \text{Binom}\left(\Delta S(t), \frac{\text{FOI}(t)}{\text{FOI}(t) + \mu}\right) \quad (\text{S39})$$

$$\Delta I(t) \sim \text{Binom}(I(t - \Delta t), 1 - \exp(-(\gamma + \mu)\Delta t)) \quad (\text{S40})$$

$$N_{IR}(t) \sim \text{Binom}\left(\Delta I(t), \frac{\gamma}{\gamma + \mu}\right) \quad (\text{S41})$$

$$\Delta R(t) \sim \text{Binom}(R(t - \Delta t), 1 - \exp(-(\delta + \mu)\Delta t)) \quad (\text{S42})$$

$$N_{RS}(t) \sim \text{Binom}\left(\Delta R(t), \frac{\delta}{\delta + \mu}\right) \quad (\text{S43})$$

$$S(t) = S(t - \Delta t) + N_{RS}(t) + B(t) - \Delta S(t) \quad (\text{S44})$$

$$I(t) = I(t - \Delta t) + N_{SI}(t) - \Delta I(t) \quad (\text{S45})$$

$$R(t) = R(t - \Delta t) + N_{IR}(t) - \Delta R(t) \quad (\text{S46})$$

⁵⁸¹ where FOI represent the force of infection; N_{ij} represent the number of individuals
⁵⁸² moving from compartment i to j on a given day; and $B(t)$ represents the number
⁵⁸³ of new births. We simulate the model on a daily scale—assuming 364 days in a
⁵⁸⁴ year so that it can be evenly grouped into 52 weeks—with the following parameters:
⁵⁸⁵ $\mathcal{R}_0 = 3$, $\theta = 0.1$, $\gamma = 1/7/\text{days}$, $\delta = 1/(364 \times 2)/\text{days}$, $\mu = 1/(364 \times 50)/\text{days}$, and
⁵⁸⁶ $N = 1 \times 10^8$. The model is simulated from 1900 to 2030 assuming $S(0) = N/3$,

⁵⁸⁷ $I(0) = 100$, and $R(0) = N - S(0) - I(0)$. The observed incidence from the model is
⁵⁸⁸ then simulated as follows:

$$C(t) = \text{Beta-Binom}(N_{SI}(t), \rho, k), \quad (\text{S47})$$

⁵⁸⁹ where ρ represents the reporting probability and k represents the overdispersion pa-
⁵⁹⁰ rameter of beta-binomial distribution. Here, we use the beta-binomial distribution to
⁵⁹¹ account for overdispersion in reporting. We assume $\rho = 0.002$ (i.e., 0.2% probability)
⁵⁹² and $k = 1000$.

⁵⁹³ We used an analogous approach for the two-strain model:

$$\beta_1(t) = b_1 \left(1 + \theta_1 \cos \left(\frac{2\pi(t - \phi_1)}{364} \right) \right) \alpha(t) \quad (\text{S48})$$

$$\beta_2(t) = b_2 \left(1 + \theta_2 \cos \left(\frac{2\pi(t - \phi_2)}{364} \right) \right) \alpha(t) \quad (\text{S49})$$

$$\text{FOI}_1(t) = \beta_1(t)(I_1(t - \Delta t) + J_1(t - \Delta t))/N \quad (\text{S50})$$

$$\text{FOI}_2(t) = \beta_2(t)(I_2(t - \Delta t) + J_2(t - \Delta t))/N \quad (\text{S51})$$

$$B(t) \sim \text{Poisson}(\mu N) \quad (\text{S52})$$

$$\Delta S(t) \sim \text{Binom}(S(t - \Delta t), 1 - \exp(-(\text{FOI}_1(t) + \text{FOI}_2(t) + \mu)\Delta t)) \quad (\text{S53})$$

$$N_{SI_1}(t) \sim \text{Binom}\left(\Delta S(t), \frac{\text{FOI}_1(t)}{\text{FOI}_1(t) + \text{FOI}_2(t) + \mu}\right) \quad (\text{S54})$$

$$N_{SI_2}(t) \sim \text{Binom}\left(\Delta S(t), \frac{\text{FOI}_2(t)}{\text{FOI}_1(t) + \text{FOI}_2(t) + \mu}\right) \quad (\text{S55})$$

$$\Delta I_1(t) \sim \text{Binom}(I_1(t - \Delta t), 1 - \exp(-(\gamma_1 + \mu)\Delta t)) \quad (\text{S56})$$

$$N_{I_1 R_1}(t) \sim \text{Binom}\left(\Delta I_1(t), \frac{\gamma_1}{\gamma_1 + \mu}\right) \quad (\text{S57})$$

$$\Delta I_2(t) \sim \text{Binom}(I_2(t - \Delta t), 1 - \exp(-(\gamma_2 + \mu)\Delta t)) \quad (\text{S58})$$

$$N_{I_2 R_2}(t) \sim \text{Binom}\left(\Delta I_2(t), \frac{\gamma_2}{\gamma_2 + \mu}\right) \quad (\text{S59})$$

$$\Delta R_1(t) \sim \text{Binom}(R_1(t - \Delta t), 1 - \exp(-(\epsilon_{21}\text{FOI}_2(t) + \rho_1 + \mu)\Delta t)) \quad (\text{S60})$$

$$N_{R_1 S}(t) \sim \text{Binom}\left(\Delta R_1(t), \frac{\rho_1}{\epsilon_{21}\text{FOI}_2(t) + \rho_1 + \mu}\right) \quad (\text{S61})$$

$$N_{R_1 J_2}(t) \sim \text{Binom}\left(\Delta R_1(t), \frac{\epsilon_{21}\text{FOI}_2(t)}{\epsilon_{21}\text{FOI}_2(t) + \rho_1 + \mu}\right) \quad (\text{S62})$$

$$\Delta R_2(t) \sim \text{Binom}(R_2(t - \Delta t), 1 - \exp(-(\epsilon_{12}\text{FOI}_1(t) + \rho_2 + \mu)\Delta t)) \quad (\text{S63})$$

$$N_{R_2 S}(t) \sim \text{Binom}\left(\Delta R_2(t), \frac{\rho_2}{\epsilon_{12}\text{FOI}_1(t) + \rho_2 + \mu}\right) \quad (\text{S64})$$

$$N_{R_2 J_1}(t) \sim \text{Binom}\left(\Delta R_2(t), \frac{\epsilon_{12}\text{FOI}_1(t)}{\epsilon_{12}\text{FOI}_1(t) + \rho_2 + \mu}\right) \quad (\text{S65})$$

$$\Delta J_1(t) \sim \text{Binom}(J_1(t - \Delta t), 1 - \exp(-(\gamma_1 + \mu)\Delta t)) \quad (\text{S66})$$

$$N_{J_1R}(t) \sim \text{Binom}\left(\Delta J_1(t), \frac{\gamma_1}{\gamma_1 + \mu}\right) \quad (\text{S67})$$

$$\Delta J_2(t) \sim \text{Binom}(J_2(t - \Delta t), 1 - \exp(-(\gamma_2 + \mu)\Delta t)) \quad (\text{S68})$$

$$N_{J_2R}(t) \sim \text{Binom}\left(\Delta J_2(t), \frac{\gamma_2}{\gamma_2 + \mu}\right) \quad (\text{S69})$$

$$\Delta R(t) \sim \text{Binom}(R(t - \Delta t), 1 - \exp(-(\rho_1 + \rho_2 + \mu)\Delta t)) \quad (\text{S70})$$

$$N_{RR_1}(t) \sim \text{Binom}\left(\Delta R(t), \frac{\rho_1}{\rho_1 + \rho_2 + \mu}\right) \quad (\text{S71})$$

$$N_{RR_2}(t) \sim \text{Binom}\left(\Delta R(t), \frac{\rho_2}{\rho_1 + \rho_2 + \mu}\right) \quad (\text{S72})$$

$$S(t) = S(t - \Delta t) - \Delta S(t) + B(t) + N_{R_1S}(t) + N_{R_2S}(t) \quad (\text{S73})$$

$$I_1(t) = I_1(t - \Delta t) - \Delta I_1(t) + N_{SI_1}(t) \quad (\text{S74})$$

$$I_2(t) = I_2(t - \Delta t) - \Delta I_2(t) + N_{SI_2}(t) \quad (\text{S75})$$

$$R_1(t) = R_1(t - \Delta t) - \Delta R_1(t) + N_{I_1R_1}(t) + N_{RR_1}(t) \quad (\text{S76})$$

$$R_2(t) = R_2(t - \Delta t) - \Delta R_2(t) + N_{I_2R_2}(t) + N_{RR_2}(t) \quad (\text{S77})$$

$$J_1(t) = J_1(t - \Delta t) - \Delta J_1(t) + N_{R_2J_1}(t) \quad (\text{S78})$$

$$J_2(t) = J_2(t - \Delta t) - \Delta J_2(t) + N_{R_1J_2}(t) \quad (\text{S79})$$

$$R(t) = R(t - \Delta t) - \Delta R(t) + N_{J_1R}(t) + N_{J_2R}(t) \quad (\text{S80})$$

594 We simulate the model on a daily scale with previously estimated parameters for the
 595 RSV-HMPV interaction [19]: $b_1 = 1.7/\text{weeks}$, $b_2 = 1.95/\text{weeks}$, $\theta_1 = 0.4$, $\theta_2 = 0.3$,
 596 $\phi_1 = 0.005 \times 7/364$, $\phi_2 = 4.99 \times 7/364$, $\epsilon_{12} = 0.92$, $\epsilon_{21} = 0.45$, $\gamma_1 = 1/10/\text{days}$,
 597 $\gamma_2 = 1/10/\text{days}$, $\rho_1 = 1/364/\text{days}$, $\rho_2 = 1/364/\text{days}$, $\mu = 1/(70 \times 364)/\text{days}$, and
 598 $N = 1 \times 10^8$. The model is simulated from 1900 to 2030 assuming $S(0) = N - 200$,
 599 $I_1(0) = 100$, $I_2(0) = 100$, $R_1(0) = 0$, $R_2(0) = 0$, $J_1(0) = 0$, $J_2(0) = 0$, and $R(0) = 0$.
 600 The observed incidence for each strain is then simulated as follows:

$$C_1(t) = \text{Beta} - \text{Binom}(N_{SI_1}(t) + N_{R_2J_1}, \rho, k), \quad (\text{S81})$$

$$C_2(t) = \text{Beta} - \text{Binom}(N_{SI_2}(t) + N_{R_1J_2}, \rho, k), \quad (\text{S82})$$

601 where ρ represents the reporting probability and k represents the overdispersion pa-
 602 rameter of beta-binomial distribution. We assume $\rho = 0.002$ (i.e., 0.2% probability)
 603 and $k = 500$. We also consider the total incidence: $C_{\text{total}}(t) = C_1(t) + C_2(t)$.

604 For both models, we consider a more realistic challenges in intervention effects
 605 $\alpha(t)$ to challenge our ability to estimate the intervention effects. Thus, we assume
 606 a 40% transmission reduction for 3 months from March 2020, followed by a 10%
 607 transmission reduction for 6 months, 20% transmission reduction for 3 months, and

608 a final return to normal levels:

$$\alpha(t) = \begin{cases} 1 & t < 2020.25 \\ 0.6 & 2020.25 \leq t < 2020.5 \\ 0.9 & 2020.5 \leq t < 2021 \\ 0.8 & 2021 \leq t < 2021.25 \\ 1 & 2021.25 \leq t \end{cases}. \quad (\text{S83})$$

609 For all simulations, we truncate the time series from the beginning of 2014 to the
610 end of 2023 and aggregate them into weekly cases.

611 To infer intrinsic resilience from time series, we fit a simple discrete time, deter-
612 ministic SIRS model [4]:

$$\Delta t = 1 \text{ week} \quad (\text{S84})$$

$$\text{FOI}(t) = \beta(t)(I(t - \Delta t) + \omega)/N \quad (\text{S85})$$

$$\Delta S(t) = [1 - \exp(-(\text{FOI}(t) + \mu)\Delta t)] S(t - \Delta t) \quad (\text{S86})$$

$$N_{SI}(t) = \frac{\text{FOI}(t)\Delta S(t)}{\text{FOI}(t) + \mu} \quad (\text{S87})$$

$$\Delta I(t) = [1 - \exp(-(\gamma + \mu)\Delta t)] I(t - \Delta t) \quad (\text{S88})$$

$$N_{IR}(t) = \frac{\gamma \Delta I(t)}{\gamma + \mu} \quad (\text{S89})$$

$$\Delta R(t) = [1 - \exp(-(\nu + \mu)\Delta t)] R(t - \Delta t) \quad (\text{S90})$$

$$N_{RS}(t) = \frac{\nu \Delta R(t)}{\nu + \mu} \quad (\text{S91})$$

$$S(t) = S(t - \Delta t) + \mu S - \Delta S(t) + N_{RS}(t) \quad (\text{S92})$$

$$I(t) = I(t - \Delta t) - \Delta I(t) + N_{SI}(t) \quad (\text{S93})$$

$$R(t) = R(t - \Delta t) - \Delta R(t) + N_{IR}(t) \quad (\text{S94})$$

613 where we include an extra term ω to account for external infections. Although actual
614 simulations do not include any external infections, we found that including this term
615 generally helped with model convergence in previous analyses [4]. The transmission
616 rate is divided into a seasonal term $\beta_{\text{seas}}(t)$ (repeated every year) and intervention
617 term $\alpha(t)$, which are estimated jointly:

$$\beta(t) = \beta_{\text{seas}}(t)\alpha(t), \quad (\text{S95})$$

618 where $\alpha < 1$ corresponds to reduction in transmission due to intervention effects. To
619 constrain the smoothness of $\beta_{\text{seas}}(t)$, we impose cyclic, random-walk priors:

$$\beta_{\text{seas}}(t) \sim \text{Normal}(\beta_{\text{seas}}(t - 1), \sigma) \quad t = 2 \dots 52 \quad (\text{S96})$$

$$\beta_{\text{seas}}(1) \sim \text{Normal}(\beta_{\text{seas}}(52), \sigma) \quad (\text{S97})$$

620 [SWP: I noticed that I forgot to put a prior on σ so need to re-do this but won't
 621 change the results.] We fix $\alpha(t) = 1$ for all $t < 2020$ and estimate α assuming a
 622 normal prior:

$$\alpha \sim \text{Normal}(1, 0.25). \quad (\text{S98})$$

623 We assume weakly informative priors on ω and ν :

$$\omega \sim \text{Normal}(0, 200) \quad (\text{S99})$$

$$\nu \sim \text{Normal}(104, 26) \quad (\text{S100})$$

624 We assume that the true birth/death rates, population sizes, and recovery rates are
 625 known. We note, however, that assuming $\gamma = 1/\text{week}$ actually corresponds to a
 626 mean simulated infectious period of 1.6 weeks, which is much longer than the true
 627 value; this approximation allows us to test whether we can still robustly estimate the
 628 intrinsic resilience given parameter mis-specification. Initial conditions are estimated
 629 with following priors:

$$S(0) = Ns(0) \quad (\text{S101})$$

$$I(0) = Ni(0) \quad (\text{S102})$$

$$s(0) \sim \text{Uniform}(0, 1) \quad (\text{S103})$$

$$i(0) \sim \text{Half-Normal}(0, 0.001) \quad (\text{S104})$$

630 Finally, the Observation model is specified as follows:

$$\text{Cases}(t) \sim \text{Negative-Binomial}(\rho N_{SI}(t), \phi) \quad (\text{S105})$$

$$\rho \sim \text{Half-Normal}(0, 0.02) \quad (\text{S106})$$

$$\phi \sim \text{Half-Normal}(0, 10) \quad (\text{S107})$$

631 where ρ represents the reporting probability and ϕ represents the negative binomial
 632 overdispersion parameter.

633 The model is fitted to four separate time series: (1) incidence time series from
 634 the SIRS model, (2) incidence time series for strain 1 from the two-strain model,
 635 (3) incidence time series for strain 2 from the two-strain model, and (4) combined
 636 incidence time series for strains 1 and 2 from the two-strain model. The model was
 637 fitted using rstan [26, 27]. The resulting posterior distribution was used to calculate
 638 the intrinsic resilience of the seasonally unforced system with the same parameters;
 639 eigenvalues of the discrete-time SIR model were computed by numerically finding
 640 the equilibrium and calculating the Jacobian matrix.

641 Validations for window-selection criteria

642 We use stochastic SIRS simulations to validate the window-selection criteria that we
 643 use for the linear regression for estimating empirical resilience. For each simulation,
 644 we begin by generating a random intervention $\alpha(t)$ from a random set of parameters.

645 First, we draw the duration of intervention τ_{npi} from a uniform distribution between
 646 0.5 and 3.5 years. Then, we draw independent normal variables z_i of length $\lfloor 364\tau_{\text{npi}} \rfloor$
 647 with a standard deviation of 0.02 and take a reverse cumulative sum to obtain a
 648 realistic shape for the intervention:

$$x_n = 1 + \sum_{i=n}^{\lfloor 364\tau_{\text{npi}} \rfloor} z_i, \quad n = 1, \dots, \lfloor 364\tau_{\text{npi}} \rfloor. \quad (\text{S108})$$

649 We repeat this random generation process until less than 10% of x_n exceeds 1. Then,
 650 we set any values that are above 1 or below 0 as 1 and 0, respectively. Then, we
 651 randomly draw the minimum transmission during intervention α_{\min} from a uniform
 652 distribution between 0.5 and 0.7 and scale x_n to have a minimum of α_{\min} :

$$x_{\text{scale},n} = \alpha_{\min} + (1 - \alpha_{\min}) \times \frac{x_n - \min x_n}{1 - \min x_n}. \quad (\text{S109})$$

653 This allows us to simulate a realistically shaped intervention:

$$\alpha(t) = \begin{cases} 1 & t < 2020 \\ x_{\text{scale},364(t-2020)} & 2020 \leq t < 2020 + \tau_{\text{npi}} \\ 1 & \tau_{\text{npi}} \leq t \end{cases}. \quad (\text{S110})$$

654 Given this intervention function, we draw \mathcal{R}_0 from a uniform distribution between 1.5
 655 and 3 and the mean duration of immunity $1/\delta$ from a uniform distribution between
 656 0.5 and 2. Then, we simulate the stochastic SIRS model from $S(0) = 10^8/\mathcal{R}_0$ and
 657 $I(0) = 100$ from 1990 to 2025 and truncate the time series to 2014–2025; if the
 658 epidemic becomes extinct before the end of simulation, we discard that simulation
 659 and start over from the intervention generation step. We then apply the window
 660 selection criteria described in the main text to compute the empirical resilience and
 661 compare it against the intrinsic resilience of the seasonally unforced system. We also
 662 compare this with the naive approach that uses the entire distance-from-attractor
 663 time series, starting from the maximum distance. We repeat this procedure 500
 664 times and quantify the correlation between empirical and intrinsic resilience estimates
 665 across two approaches.

Supplementary Figures

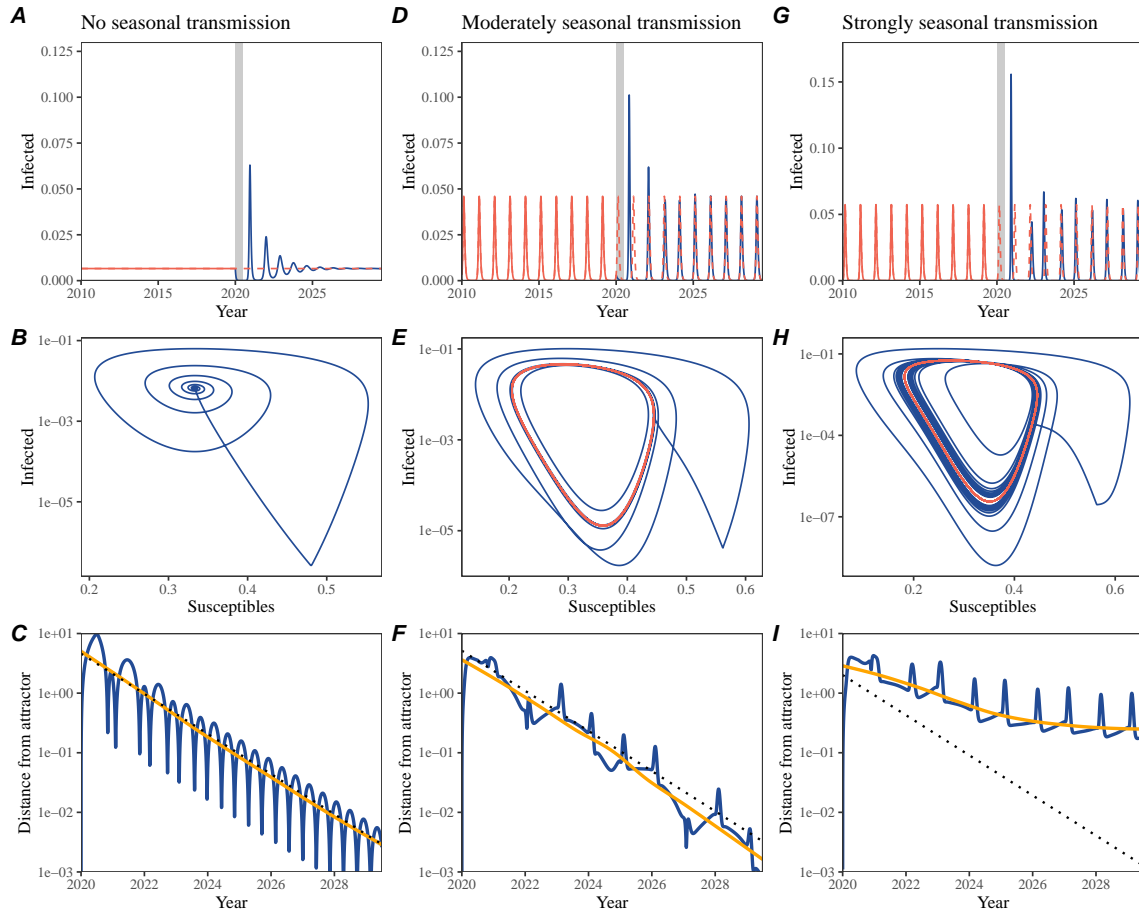


Figure S1: Impact of seasonal transmission on pathogen resilience. (A, D, G) Simulated epidemic trajectories using the SIRS model without seasonal forcing (A), with seasonal forcing of amplitude of 0.2 (D), and with seasonal forcing of amplitude of 0.4 (G). Red and blue solid lines represent epidemic dynamics before and after interventions are introduced, respectively. Red dashed lines represent counterfactual epidemic dynamics in the absence of interventions. Gray regions indicate the duration of interventions. (B, E, H) Phase plane representation of the corresponding model. Red and blue solid lines represent epidemic trajectories on an SI phase plane before and after interventions are introduced, respectively. (C, F, I) Changes in logged distance from the attractor over time. Blue lines represent the logged distance from the attractor. Orange lines represent the locally estimated scatterplot smoothing (LOESS) fits to the logged distance from the attractor. Dotted lines are superimposed as a comparison to have the same slope as the intrinsic resilience of the seasonally unforced system.

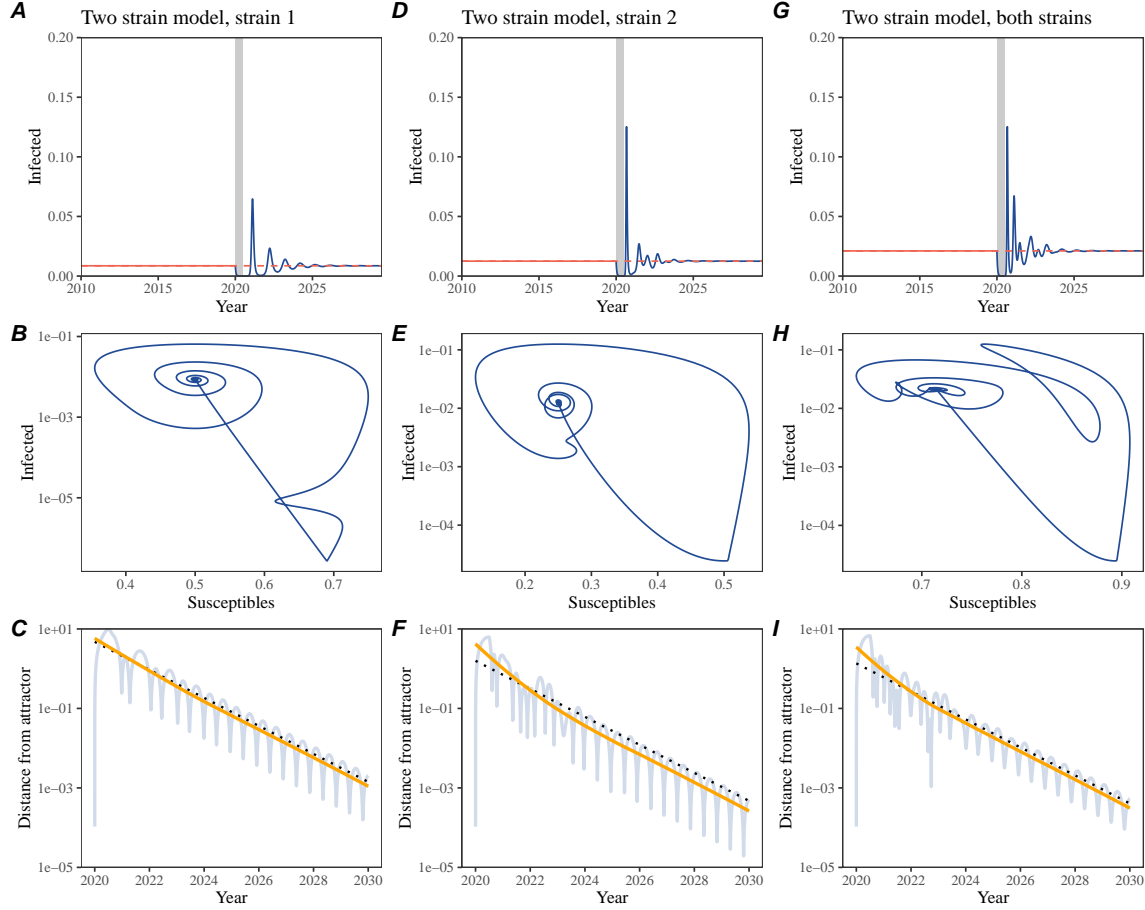


Figure S2: Conceptual framework for measuring pathogen resilience following NPIs for a two-strain system without seasonal forcing. (A, D, G) Simulated epidemic trajectories using a multi-strain system without seasonal forcing. Red and blue solid lines represent epidemic dynamics before and after interventions are introduced, respectively. Red dashed lines represent counterfactual epidemic dynamics in the absence of interventions. Gray regions indicate the duration of interventions. (B, E, H) Phase plane representation of the corresponding model. Blue solid lines represent epidemic trajectories on an SI phase plane before and after interventions are introduced, respectively. (C, F, I) Changes in logged distance from the attractor over time. Blue lines represent the logged distance from the attractor. Orange lines represent the locally estimated scatterplot smoothing (LOESS) fits to the logged distance from the attractor. Dotted lines are superimposed as a comparison to have the same slope as the intrinsic resilience of the seasonally unforced system.

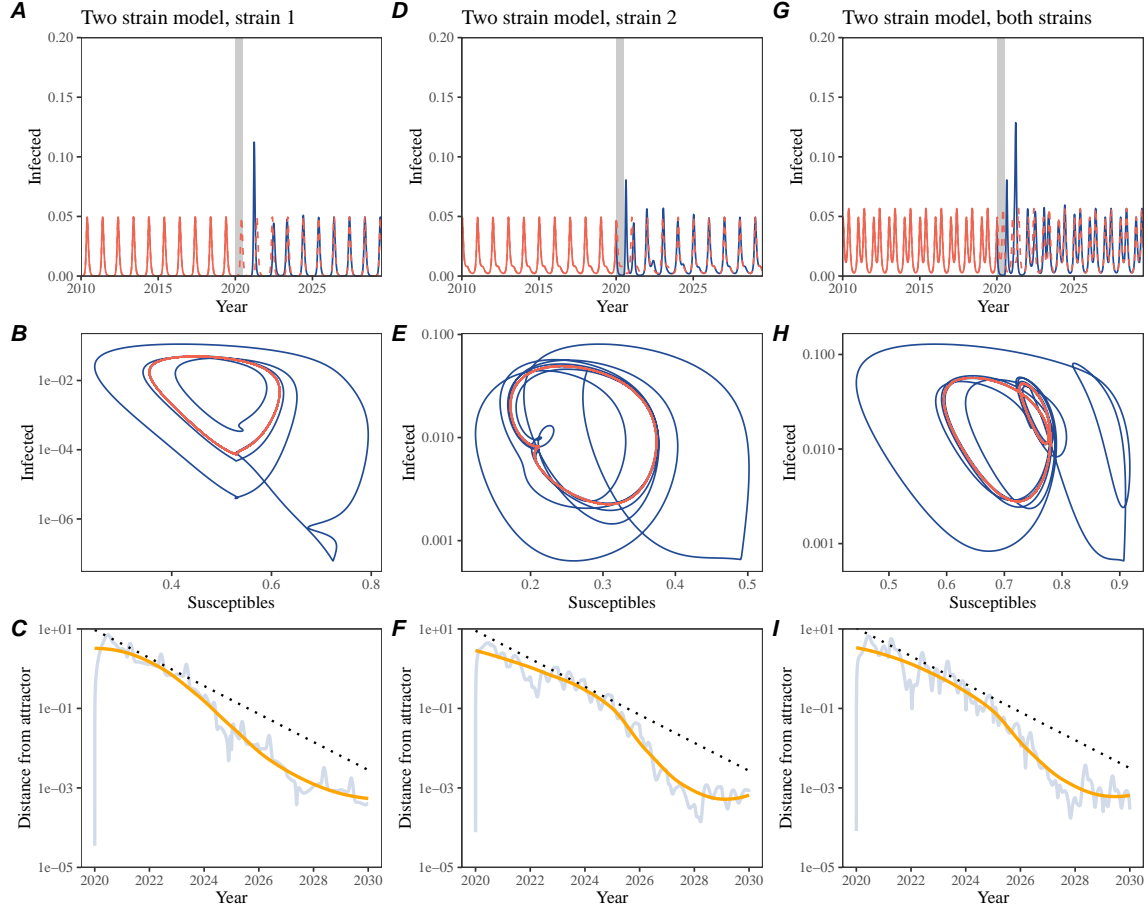


Figure S3: Conceptual framework for measuring pathogen resilience following NPIs for a multi-strain system with seasonal forcing. (A, D, G) Simulated epidemic trajectories using a multi-strain system with seasonal forcing (amplitude of 0.2). Red and blue solid lines represent epidemic dynamics before and after interventions are introduced, respectively. Red dashed lines represent counterfactual epidemic dynamics in the absence of interventions. Gray regions indicate the duration of interventions. (B, E, H) Phase plane representation of the corresponding model. Red and blue solid lines represent epidemic trajectories on an SI phase plane before and after interventions are introduced, respectively. (C, F, I) Changes in logged distance from the attractor over time. Blue lines represent the logged distance from the attractor. Orange lines represent the locally estimated scatterplot smoothing (LOESS) fits to the logged distance from the attractor. Dotted lines are superimposed as a comparison to have the same slope as the intrinsic resilience of the seasonally unforced system.

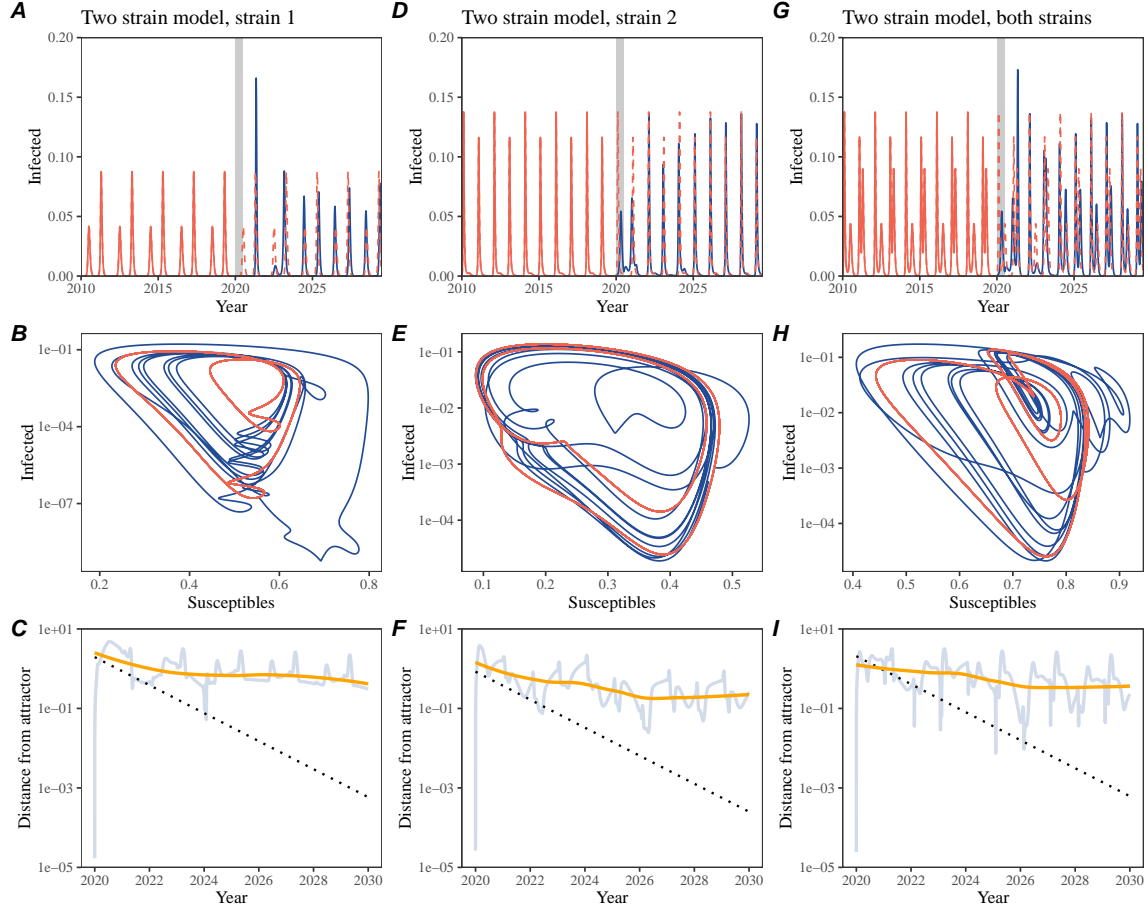


Figure S4: Conceptual framework for measuring pathogen resilience following NPIs for a multi-strain system with strong seasonal forcing. (A, D, G) Simulated epidemic trajectories using a multi-strain system with seasonal forcing (amplitude of 0.4). Red and blue solid lines represent epidemic dynamics before and after interventions are introduced, respectively. Red dashed lines represent counterfactual epidemic dynamics in the absence of interventions. Gray regions indicate the duration of interventions. (B, E, H) Phase plane representation of the corresponding model. Red and blue solid lines represent epidemic trajectories on an SI phase plane before and after interventions are introduced, respectively. (C, F, I) Changes in logged distance from the attractor over time. Blue lines represent the logged distance from the attractor. Orange lines represent the locally estimated scatterplot smoothing (LOESS) fits to the logged distance from the attractor. Dotted lines are superimposed as a comparison to have the same slope as the intrinsic resilience of the seasonally unforced system.

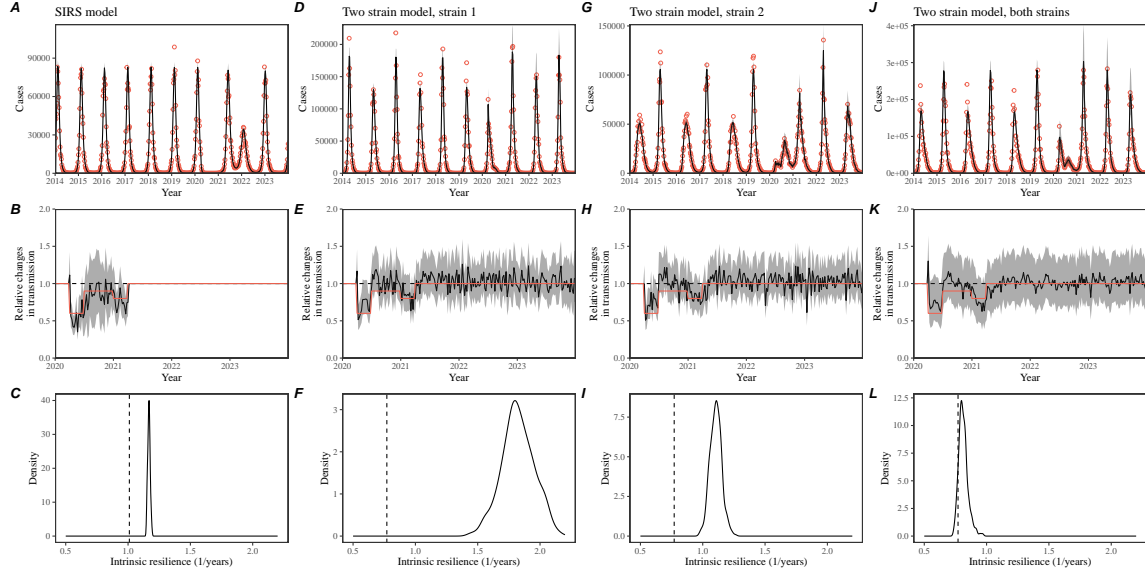


Figure S5: Mechanistic model fits to simulated data and inferred intrinsic resilience. (A, D, G, J) Simulated case time series from corresponding models (red) and SIRS model fits (black). (B, E, H, K) Assumed changes in transmission due to pandemic NPIs (red) and estimated changes from the SIRS model (black). Solid lines and shaded regions represent fitted posterior median and 95% credible intervals. (C, F, I, L) True intrinsic resilience of the seasonally unforced system (vertical lines) and the posterior distribution of the inferred intrinsic resilience from the SIRS model (density plots).

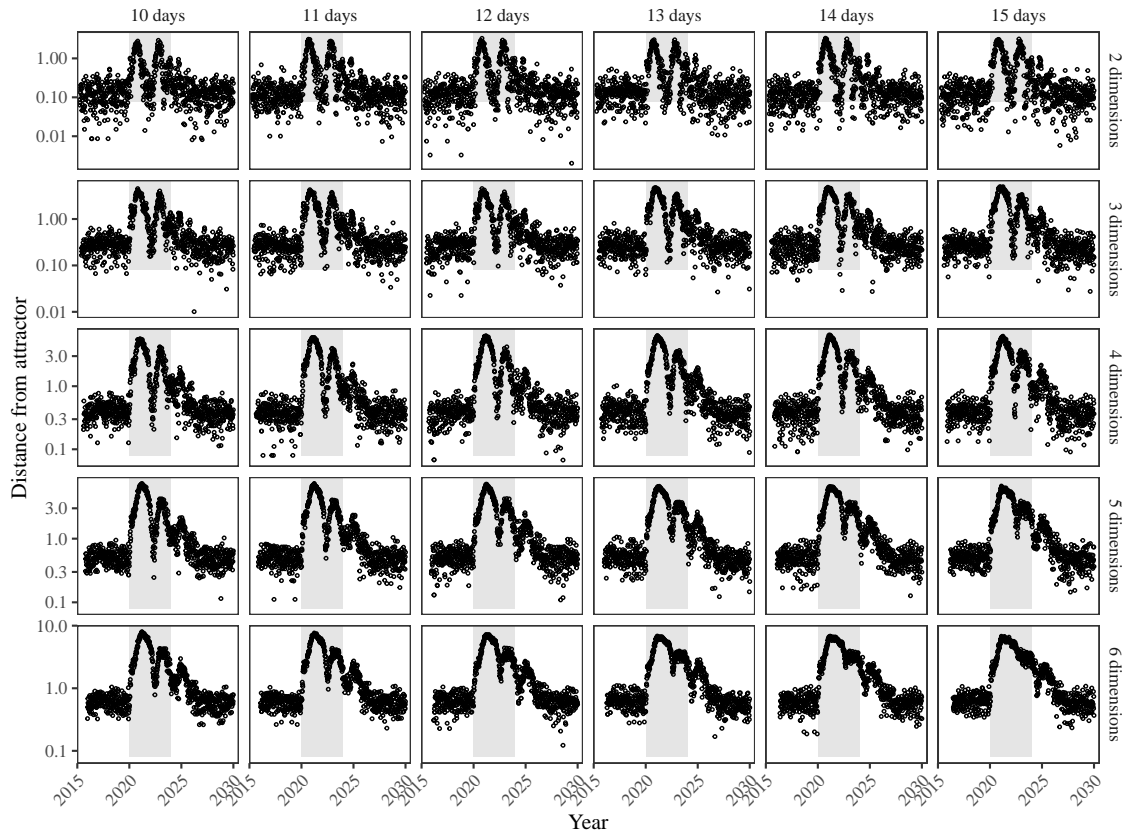


Figure S6: Sensitivity of the distance from the attractor to choices about embedding lags and dimensions. Sensitivity analysis for the distance-from-attractor time series shown in Figure 3E in the main text by varying the embedding lag between 10–15 days and embedding dimensions between 2–6 dimensions.

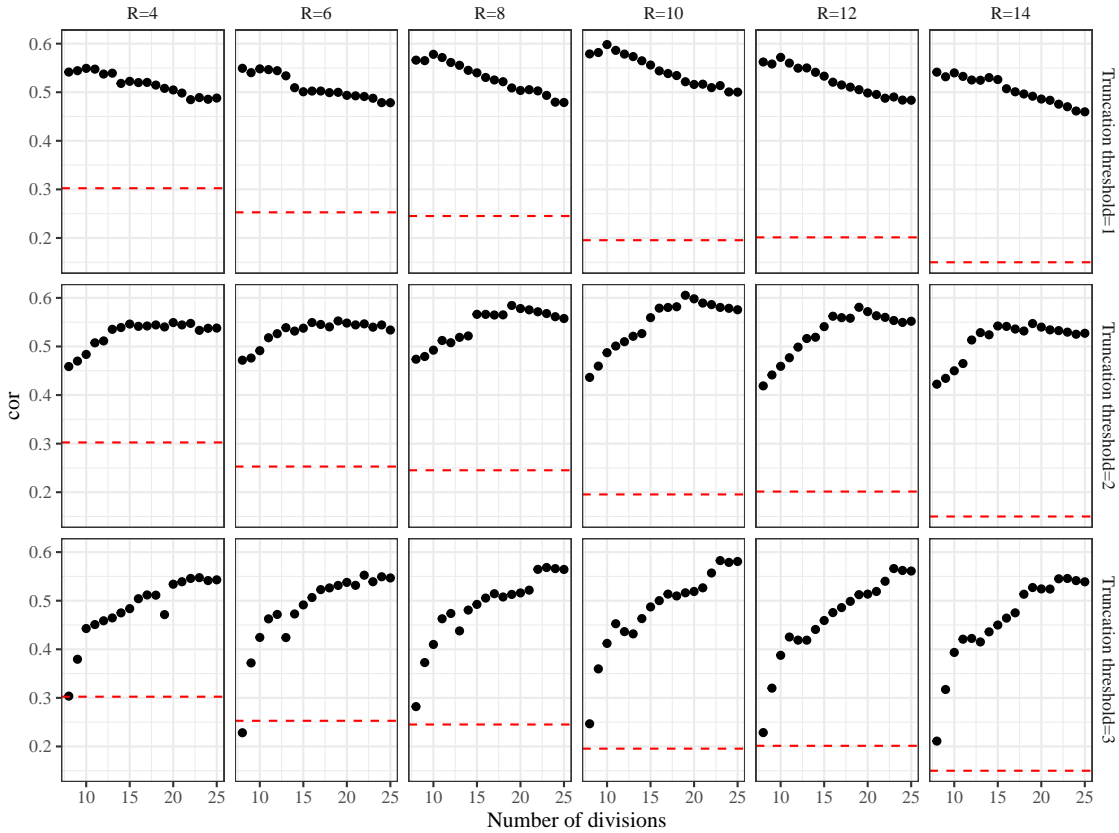


Figure S7: Impact of fitting window selection on the estimation of empirical resilience. We simulated 500 epidemics of a stochastic SIRS model with randomly drawn parameters and randomly generated intervention impacts. For each simulation, we reconstructed the empirical attractor based on the approach outlined in Figure 3 and estimate the distance from the attractor. The naive approach fits a linear regression on a log scale, starting from the maximum distance until the end of the time series. The window-based approach tries to select an appropriate window by smoothing the distance estimates and finding the time period when the smoothed time series crosses pre-determined threshold, relative to the maximum distance; then, a linear regression is fitted by using the raw distance within this time period.

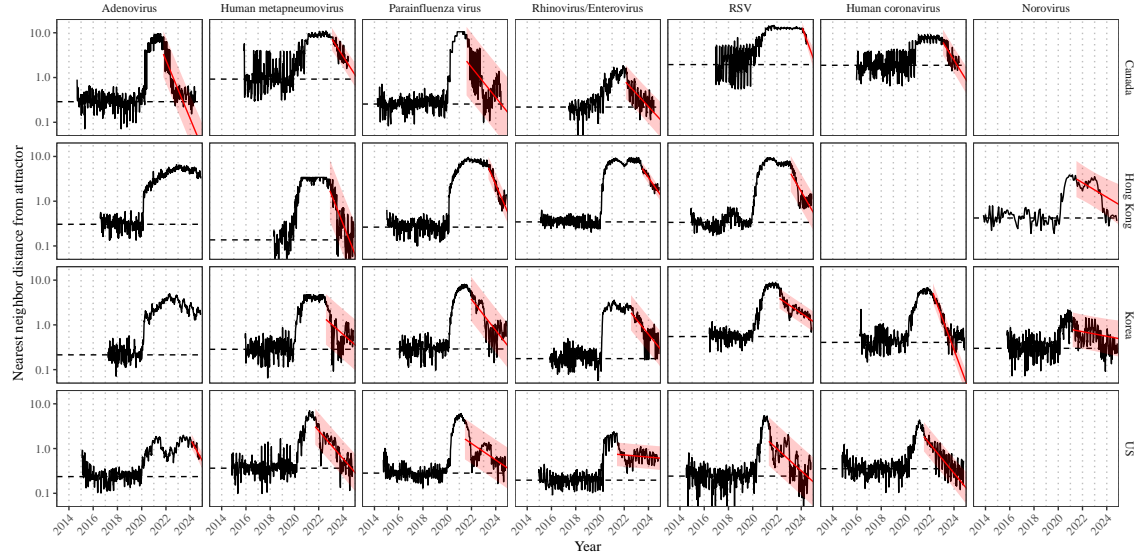


Figure S8: Estimated time series of distance from the attractor for each pathogen and corresponding linear regression fits using automated window selection criterion across Canada, Hong Kong, Korea, and the US. Black lines represent the estimated distance from the attractor. Red lines and shaded regions represent the linear regression fits and corresponding 95% confidence intervals. Dashed lines represent the average of the pre-pandemic nearest neighbor distances.

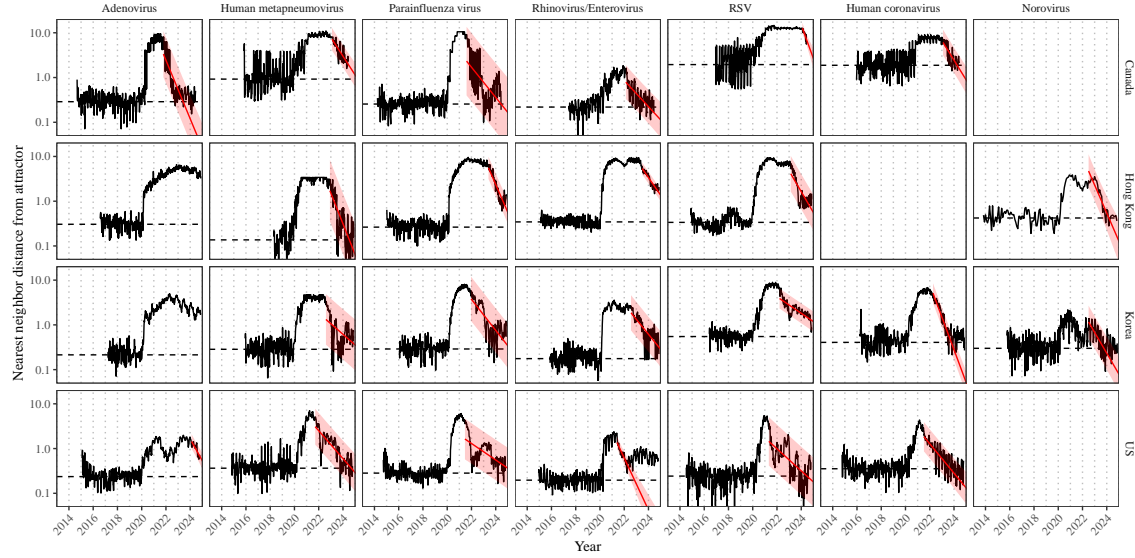


Figure S9: Estimated time series of distance from the attractor for each pathogen and corresponding linear regression fits across Canada, Hong Kong, Korea, and the US, including ad-hoc regression window selection. We used ad-hoc regression windows for norovirus in Hong Kong and Korea and Rhinovirus/Enterovirus in the US. Black lines represent the estimated distance from the attractor. Red lines and shaded regions represent the linear regression fits and corresponding 95% confidence intervals. Dashed lines represent the average of the pre-pandemic nearest neighbor distances.

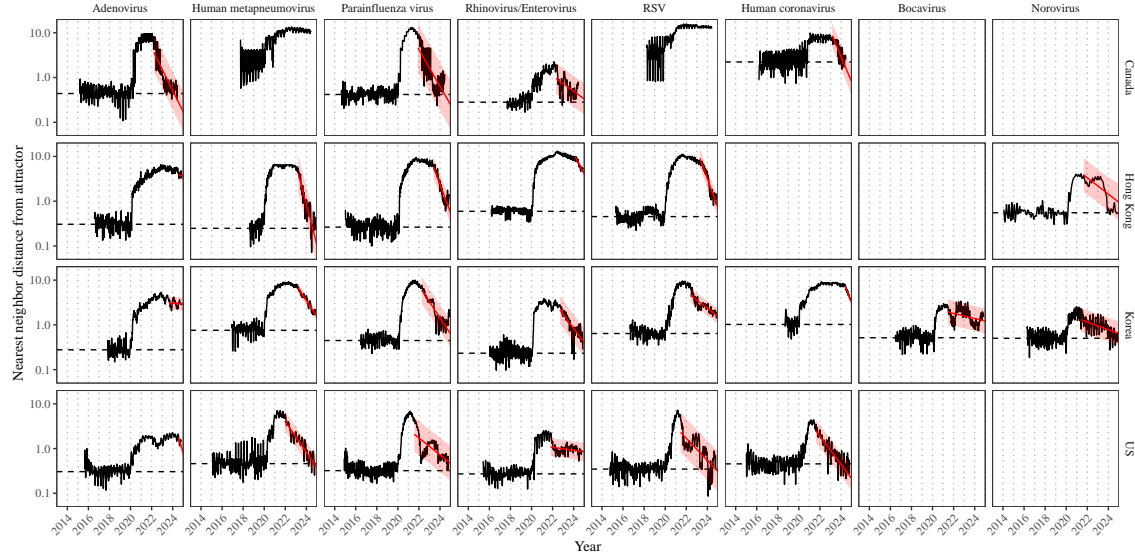


Figure S10: Estimated time series of distances from the attractor for each pathogen across Canada, Hong Kong, Korea, and the US using higher embedding dimensions. Black lines represent the estimated distance from the attractor. Red lines and shaded regions represent the linear regression fits and corresponding 95% confidence intervals. Dashed lines represent the average of the pre-pandemic nearest neighbor distances. A lower threshold is used for determining embedding dimensions with the false nearest neighbors approach, thereby yielding a higher embedding dimension.

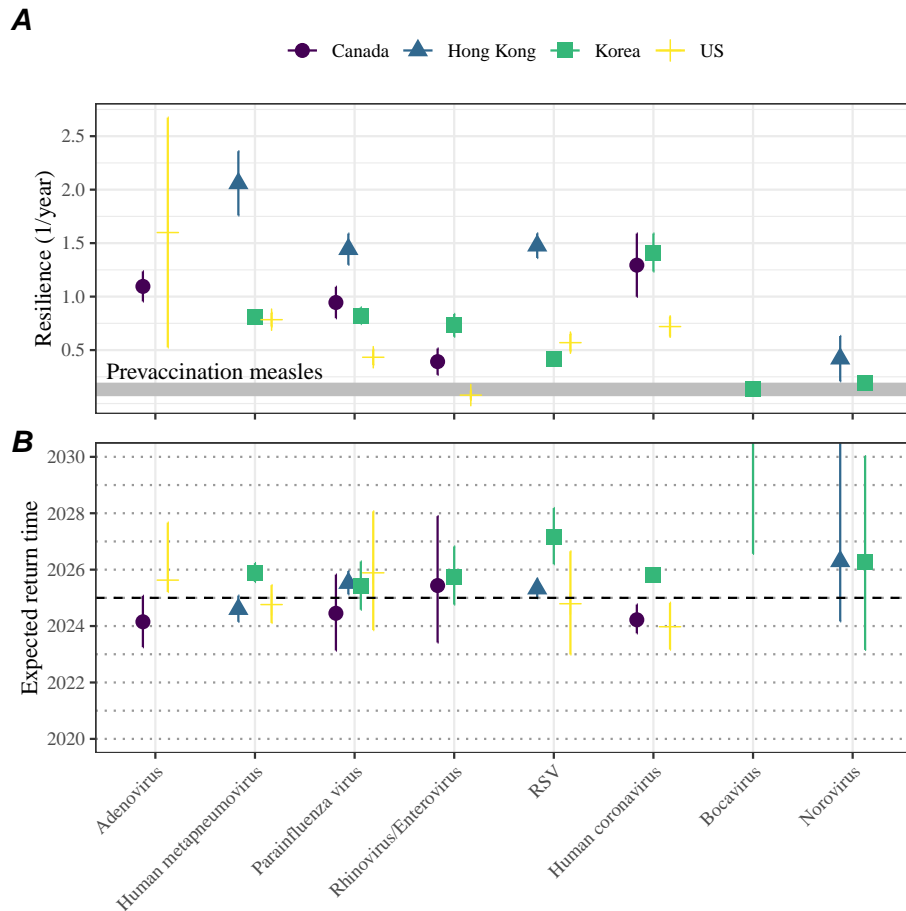


Figure S11: Summary of resilience estimates using higher embedding dimensions. (A) Estimated pathogen resilience. The gray horizontal line represents the intrinsic resilience of pre-vaccination measles dynamics. (B) Predicted timing of when each pathogen will return to their pre-pandemic cycles. The dashed line in panel B indicates the end of 2024 (current observation time). Error bars represent 95% confidence intervals. A lower threshold is used for determining embedding dimensions with the false nearest neighbors approach, thereby yielding a higher embedding dimension.

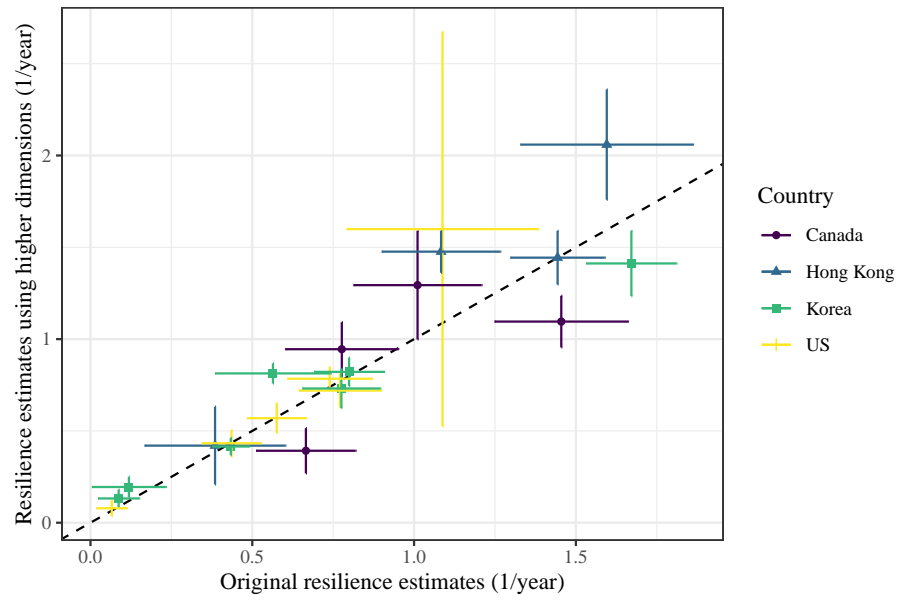


Figure S12: **Comparison of resilience estimates.** Each point represents a resilience estimate for a specific pathogen at a specific country. The x values represent the original resilience estimates presented in Figure 4. The y values represent the original resilience estimates presented in Supplementary Figure S11.

667 **References**

- 668 [1] Rachel E Baker, Sang Woo Park, Wenchang Yang, Gabriel A Vecchi, C Jessica E
669 Metcalf, and Bryan T Grenfell. The impact of COVID-19 nonpharmaceutical
670 interventions on the future dynamics of endemic infections. *Proceedings of the*
671 *National Academy of Sciences*, 117(48):30547–30553, 2020.
- 672 [2] Gabriela B Gomez, Cedric Mahé, and Sandra S Chaves. Uncertain effects of the
673 pandemic on respiratory viruses. *Science*, 372(6546):1043–1044, 2021.
- 674 [3] Mihaly Koltai, Fabienne Krauer, David Hodgson, Edwin van Leeuwen, Marina
675 Treskova-Schwarzbach, Mark Jit, and Stefan Flasche. Determinants of RSV
676 epidemiology following suppression through pandemic contact restrictions. *Epi-*
677 *demics*, 40:100614, 2022.
- 678 [4] Sang Woo Park, Brooklyn Noble, Emily Howerton, Bjarke F Nielsen, Sarah
679 Lentz, Lilliam Ambroggio, Samuel Dominguez, Kevin Messacar, and Bryan T
680 Grenfell. Predicting the impact of non-pharmaceutical interventions against
681 COVID-19 on *Mycoplasma pneumoniae* in the United States. *Epidemics*,
682 49:100808, 2024.
- 683 [5] Amanda C Perofsky, Chelsea L Hansen, Roy Burstein, Shanda Boyle, Robin
684 Prentice, Cooper Marshall, David Reinhart, Ben Capodanno, Melissa Truong,
685 Kristen Schwabe-Fry, et al. Impacts of human mobility on the citywide trans-
686 mission dynamics of 18 respiratory viruses in pre-and post-COVID-19 pandemic
687 years. *Nature communications*, 15(1):4164, 2024.
- 688 [6] Eric J Chow, Timothy M Uyeki, and Helen Y Chu. The effects of the COVID-19
689 pandemic on community respiratory virus activity. *Nature Reviews Microbiol-*
690 *ogy*, 21(3):195–210, 2023.
- 691 [7] Stephen M Kissler, Christine Tedijanto, Edward Goldstein, Yonatan H Grad,
692 and Marc Lipsitch. Projecting the transmission dynamics of SARS-CoV-2
693 through the postpandemic period. *Science*, 368(6493):860–868, 2020.
- 694 [8] Rachel E Baker, Chadi M Saad-Roy, Sang Woo Park, Jeremy Farrar, C Jessica E
695 Metcalf, and Bryan T Grenfell. Long-term benefits of nonpharmaceutical inter-
696 ventions for endemic infections are shaped by respiratory pathogen dynamics.
697 *Proceedings of the National Academy of Sciences*, 119(49):e2208895119, 2022.
- 698 [9] John-Sebastian Eden, Chisha Sikazwe, Ruopeng Xie, Yi-Mo Deng, Sheena G
699 Sullivan, Alice Michie, Avram Levy, Elena Cutmore, Christopher C Blyth,
700 Philip N Britton, et al. Off-season RSV epidemics in Australia after easing
701 of COVID-19 restrictions. *Nature communications*, 13(1):2884, 2022.
- 702 [10] Stuart L Pimm. The structure of food webs. *Theoretical population biology*,
703 16(2):144–158, 1979.

- 704 [11] Michael G Neubert and Hal Caswell. Alternatives to resilience for measuring
705 the responses of ecological systems to perturbations. *Ecology*, 78(3):653–665,
706 1997.
- 707 [12] Lance H Gunderson. Ecological resilience—in theory and application. *Annual
708 review of ecology and systematics*, 31(1):425–439, 2000.
- 709 [13] Vasilis Dakos and Sonia Kéfi. Ecological resilience: what to measure and how.
710 *Environmental Research Letters*, 17(4):043003, 2022.
- 711 [14] Floris Takens. Detecting strange attractors in turbulence. In *Dynamical Sys-
712 tems and Turbulence, Warwick 1980: proceedings of a symposium held at the
713 University of Warwick 1979/80*, pages 366–381. Springer, 2006.
- 714 [15] Jonathan Dushoff, Joshua B Plotkin, Simon A Levin, and David JD Earn. Dynamical resonance can account for seasonality of influenza epidemics. *Pro-
715 ceedings of the National Academy of Sciences*, 101(48):16915–16916, 2004.
- 716 [16] Alan Hastings, Karen C Abbott, Kim Cuddington, Tessa Francis, Gabriel Gell-
717 ner, Ying-Cheng Lai, Andrew Morozov, Sergei Petrovskii, Katherine Scran-
718 ton, and Mary Lou Zeeman. Transient phenomena in ecology. *Science*,
719 361(6406):eaat6412, 2018.
- 720 [17] Matthew B Kennel, Reggie Brown, and Henry DI Abarbanel. Determining
721 embedding dimension for phase-space reconstruction using a geometrical con-
722 struction. *Physical review A*, 45(6):3403, 1992.
- 723 [18] Eugene Tan, Shannon Algar, Débora Corrêa, Michael Small, Thomas Stemler,
724 and David Walker. Selecting embedding delays: An overview of embedding
725 techniques and a new method using persistent homology. *Chaos: An Interdis-
726 ciplinary Journal of Nonlinear Science*, 33(3), 2023.
- 727 [19] Samit Bhattacharyya, Per H Gesteland, Kent Korgenski, Ottar N Bjørnstad,
728 and Frederick R Adler. Cross-immunity between strains explains the dynamical
729 pattern of paramyxoviruses. *Proceedings of the National Academy of Sciences*,
730 112(43):13396–13400, 2015.
- 731 [20] Bryan T Grenfell, Ottar N Bjørnstad, and Bärbel F Finkenstädt. Dynamics of
732 measles epidemics: scaling noise, determinism, and predictability with the TSIR
733 model. *Ecological monographs*, 72(2):185–202, 2002.
- 734 [21] Virginia E Pitzer, Cécile Viboud, Vladimir J Alonso, Tanya Wilcox, C Jessica
735 Metcalf, Claudia A Steiner, Amber K Haynes, and Bryan T Grenfell. Environ-
736 mental drivers of the spatiotemporal dynamics of respiratory syncytial virus in
737 the United States. *PLoS pathogens*, 11(1):e1004591, 2015.

- 739 [22] Katharine R Dean, Fabienne Krauer, Lars Walløe, Ole Christian Lingjærde, Bar-
740 bara Bramanti, Nils Chr Stenseth, and Boris V Schmid. Human ectoparasites
741 and the spread of plague in Europe during the Second Pandemic. *Proceedings*
742 *of the National Academy of Sciences*, 115(6):1304–1309, 2018.
- 743 [23] Margarita Pons-Salort and Nicholas C Grassly. Serotype-specific immunity
744 explains the incidence of diseases caused by human enteroviruses. *Science*,
745 361(6404):800–803, 2018.
- 746 [24] Sarah Cobey and Edward B Baskerville. Limits to causal inference with state-
747 space reconstruction for infectious disease. *PLoS one*, 11(12):e0169050, 2016.
- 748 [25] Edward Goldstein, Sarah Cobey, Saki Takahashi, Joel C Miller, and Marc Lip-
749 sitch. Predicting the epidemic sizes of influenza A/H1N1, A/H3N2, and B: a
750 statistical method. *PLoS medicine*, 8(7):e1001051, 2011.
- 751 [26] Bob Carpenter, Andrew Gelman, Matthew D Hoffman, Daniel Lee, Ben
752 Goodrich, Michael Betancourt, Marcus A Brubaker, Jiqiang Guo, Peter Li,
753 and Allen Riddell. Stan: A probabilistic programming language. *Journal of*
754 *statistical software*, 76, 2017.
- 755 [27] Stan Development Team. RStan: the R interface to Stan, 2024. R package
756 version 2.32.6.